ELECTROCHEMSITRY AND SPINTRONICS OF GRAPHENE

A Dissertation

Presented to the Faculty of the Graduate School

of Cornell University

In Partial Fulfillment of the Requirements for the Degree of

Doctor of Philosophy

by

Wan Li

August 2013

ELECTROCHEMSITRY AND SPINTRONICS OF GRAPHENE

Wan Li, Ph. D.

Cornell University 2013

Graphene is the name given to a monolayer of carbon atoms that are tightly packed into a two-dimensional honeycomb lattice. Since experimentally isolated in 2004, graphene has attracted widespread research interests for its outstanding electrical, optical, mechanical and thermal properties. The main theme of my doctoral research is to investigate the properties and potential applications of this magic material in electrochemistry and spintronics.

In the first study, we investigated the electrochemistry of individual monolayer graphene. In particular, we fabricated devices in which a well-defined area of monolayer graphene served as the working electrode in electrochemical experiments. We examined both mechanically exfoliated graphene and graphene grown by chemical vapor deposition, with a focus on the interaction between graphene and the simple redox molecule ferrocenemethanol. We found the electron transfer rate of ferrocenemethanol at both types of graphene electrodes to be more than 10-fold faster than that at the basal plane of graphite, which we ascribed to corrugations in the graphene surfaces. We further demonstrated that molecule adsorption and desorption on graphene surface can be detected in real-time with electrochemistry techniques.

In the second study, we explored the potential applications of graphene as a barrier material in magnetic tunnel junctions (MTJs). We developed a novel fabrication process that aimed to make graphene-based magnetic junctions with no oxidation of the ferromagnetic material (FM) at the FM/graphene interfaces. The oxidation issue was hard to avoid in traditional graphene fabrication processes, and may have accounted for the extremely large resistance-area (*RA*) products in previously reported graphene-based MTJs. Electrical characterization of our junction devices indicates that the junctions are tunnel junctions with 1-4% magnetoresistance and low *RA* products of 3-10 $\Omega\mu m^2$. These *RA* values are $\sim 10^4$ times smaller than previous results, suggestive of intrinsic FM/graphene interfaces without oxidation.

BIOGRAPHICAL SKETCH

Wan Li was born on March 8th, 1982 in Lin-yi, a small town in China. Six months later, she moved to Lang-fang, another small town in Hebei, China, where she felt so blessed to grow up with her grandparents. Wan's earliest science education started on the backseat of her grandfather's bicycle, where her grandfather, a well-respected physician, discussed a lot of interesting "science" topics (*e.g.,* Why is there wind? Why do people use transformers?) with Wan (who was then no more than 5-year old), through effective solid-borne sound transmission.* Wan's grandmother was not able to enter middle school in her youth, but she taught herself well and insisted on all her children and grandchildren getting high-level education. She encouraged Wan to never be satisfied by the knowledge that she currently gained, and spent numerous weekends with Wan in libraries and bookstores digging for knowledge from books. At the age of 17, Wan was one of the two girls who ranked top 20 in the Physics Olympic Competition for High School Students in the Hebei Province.

At the age of 18, Wan entered Tsinghua University to continue her education, initially as an engineering-majored college student. She then decided to follow her heart and transferred to physics major in the 3rd year of her college. Wan was thereafter exposed to scientific research in Prof. Yong Guo's group and got the chance to know Ke Xu (her lifelong love), which together led to the turning point of her life: continuing the science career by applying to graduate schools across the ocean. Before

*This was realized simply by putting Wan's ear on her grandfather's back.

this point, Wan obtained both Bachelor of Science degree (with honor) and Master degree in Physics at Tsinghua University in 2005 and 2007, respectively. She also got her theoretical study on time-domain spin-dependent transport published in *Physical Review B* in 2006.

Wan started her graduate study in the Physics Department at Cornell University in 2007, and got extremely lucky to join Prof. Dan Ralph's group in 2008. Since then, she started the journey to experimentally study the properties of graphene in electrochemistry and spintronics under Dan and Prof. Héctor Abruña's guidance. Wan's next stop will be a postdoc position in Prof. Jay Groves' lab at UC Berkeley, where she will explore the possibility of integrating graphene with bio-systems.

To my beloved grandparents and husband, for their love and support

我爱你们，亲爱的外公外婆和先生

ACKNOWLEDGMENTS

Six years of graduate study is like a journey for me. I would not have come to this point without the help from so many people. It's so nice that I have this opportunity to express my deep gratitude to all the people who have encouraged, helped, and supported me along the journey.

First and foremost, I'd like to thank my advisor, Prof. Dan Ralph, for his consistent support all through my graduate study. Being a great scientist and a field leader himself, Dan makes graduate student education his career priority. He builds up a great lab with abundant resources, and provides us with great research ideas while leaving us the freedom to pursue other interesting topics. Moreover, Dan always makes himself available for discussions and even hands-on instructions, which solved many of my problems in experiments and taught me how to think and work as a good scientist. Moreover, as an international student who is not a native English speaker and has an intrinsic silent nature, I am also very grateful to Dan for his patience in communicating with me, as well as his efforts in improving my English writing and presentation skills. Overall, I feel really privileged to be Dan's student, and any language would be far from enough to express my deep gratitude to him.

I am also extremely grateful to Prof. Héctor Abruña, who opened my vision to electrochemistry-a wonderful field that's different from my major. I got to know Prof. Abruña in the winter of 2008 when I started my first independent project. Since then, I was so lucky to be able to meet with Prof. Abruña in *small group meetings* every week, and get tons of insightful advises that made my research life much easier. I am

really impressed by Prof. Abruña's enthusiasm on science and how knowledgeable he is in almost every field, including chemistry, physics, material science, and even music and art. Prof. Abruña also provided great guidance to Ke Xu, my husband, throughout his faculty application process. All these, we appreciate so much!

I would like to thank Prof. James Sethna for being my committee member. In particular, I got very helpful discussions with him during my A-exam. Prof. Sethna is very rigorous in science. The discussions with him helped me deepen my understanding on the origin of high mobility, valley transport, and the backscattering suppression of graphene from a theoretical perspective.

I would like to thank Prof. Paul McEuen for being my first-year committee member and enlightening me through very productive discussions. He also kindly introduced me to his lab members, from whom I learnt how to handle graphene. Moreover, he is very generous in letting me use his lab equipment for various experiments.

I would like to thank Prof. Louis Hand for his kind guidance during my first year at Cornell, which helped me greatly to adapt to the graduate student life at Cornell. I'd also like to thank many other Cornell professors during my graduate school years, in particular Prof. Piet Brouwer, Prof. Robert Buhrman, Prof. William Dichtel, Prof. David Muller, Prof. Jiwoong Park, Prof. Ritchie Patterson, and Prof. Albert Sievers.

I am also very grateful to the whole Ralph group. Sufei Shi was the first Ralph group student with whom I worked. He taught me a tremendous amount of lab skills. Personally, he is a great friend to me who always helps me with both my experiments and everyday life, even after his graduation. Eugenia Tam is an "angel" in the Ralph group; it was a wonderful experience for me to work with her on the graphene spin Hall project. She is very good at data interpretation and taught me a lot on electrical measurements. Lin Xue was one of my closest friends in Ralph group. We enjoy a lot of the TGIF chips together. In research, he provided me with many helpful suggestions on my graphene magnetic junction project. Yongtao Cui, Joshua Parks, and Chen Wang are all super smart; I feel it's my privilege to work with them in the same group. Kiran Thadani was my lovely officemate. I was impressed by her kindness and sweetness to everybody, which makes the group more like a family. I also want to thank Alex Mellnik for generously lending his PPMS external measurement setup to Eugenia and me for our graphene spin Hall effect project, Colin Heikes for his expertise in material science and help with Sharon maintenance, and Greg Stiehl for his help with Sharon maintenance. I would also like to thank other previous and current group members: Dr. Saikat Ghosh, Dr. Takahiro Moriyama, Ted Gudmundsen, Jennifer Grab, David MacNeill, Colin Jermain, Neal Reynolds and Jonathan Gibbons.

The highly collaborative environment at Cornell enabled me to work with and get help from many graduate students and postdocs from other groups. I am particularly grateful to Joanna (Cen) Tan from Prof. Abruña's group, with whom I worked on the graphene-electrochemistry project. Joanna is extremely smart and considerate. I feel very lucky to be able to work with her. Our collaboration not only

led us to success of the project but also a great friendship through these years. I'd also like to thank Michael Lowe for helping me with the electrochemical experiments using exfoliated graphene electrodes, and Joaquin Redrigues-Lopez, Nicole Ritzert, Mitk'El B. Santiago-Berrios, Michelle Tague, Deli Wang and Yu-wu Zhong, for their friendship and kind helps. They are all from Prof. Abruña's group. I also obtained great help from people in Prof. McEuen's lab. In particular, Arend van der Zande showed me how to prepare both exfoliated and chemical vapored deposited (CVD) graphene. Samantha Roberts guided me through the general fabrication process for CVD graphene. Besides, Samantha's 100% optimistic attitude is always encouraging to me. I am also grateful for Yaqiong Xu and Xiaodong Xu for their great friendship. In Prof. Jiwoong Park's group, Zenghui Wang helped me in examining CVD graphene samples with dark-field TEM. Mark Levendorf provided me with the first batch of CVD graphene samples before I could grow them by myself. In Prof. David Muller's group, Pinshane Huang showed Joanna and me how to do dark-field TEM on graphene. I also got very helpful discussions with Praveen Gowtham, Yun Li, Luqiao Liu, and Chi-feng Pai in Prof. Buhrman's group. I really appreciate their help and friendship during these years.

I want to thank all the terrific support I have received from Steve Kriske, Eric Smith, Jon Shu, Mick Thomas, and Prof. Christopher Umbach at CCMR, Nate Ellis and Rodney Bowman at the machine shop, and all the staff members at CNF and NBTC. They have been great sources of information and extremely helpful in different areas of my research.

I am also grateful to my other friends at Cornell with whom I shared precious memories. Among them, Xin Shi was my first year graduate student mentor and was a true big brother for me who was always ready to offer help. Yao Weng, Peijun Zhou, and Qingyun Mao were my roommates and sweetest friends. Yang Xie is a great guy who organized many fun parties. Paul Zhu is the coolest person who took me fly over the Cayuga Lake and let me operate the flight for a minute. And also Yong Chen, Yi Jing, Heng Li, Hui Liu, Tchefor Ndnukum, Yongxi Ou, Meng Wang, Saien Xie, Huolin Xin, and Ying Zheng. I want to say thank you for your friendship all through these years.

I reserve the last paragraph to express my deep gratitude to my family, in particular, my grandparents who raised me up with their unconditional love. The love never decreased over years, nor blocked by the 7,000-mile distance between US and China. In the meantime, I really want to apologize for not being able to be with them during these years. I also want to thank my parents for taking care of my beloved grandparents, and my parents-in laws for seeing me as their own daughter. And now, I want to turn to my husband, Ke Xu, whom I see as my soul mate and the magic in life. For all the years we know each other, Ke fills my heart with love by his consistent care and support; draws in my mind a beautiful picture (憧憬) of our future; and works extremely hard to realize it step by step. Dear Ke, thank you so much for what you have done for me. I love you!

TABLE OF CONTENTS

LIST OF FIGURES

LIST OF TABLES

CHAPTER 1

INTRODUCTION

1.1 Graphene: The Main Theme of My Doctoral Research

Graphene is the name given to a monolayer of carbon atoms tightly packed into a two-dimensional (2D) honeycomb lattice [Figure 1.1(a)]. Although it was historically presumed to be unstable in free-standing state (*1*), graphene was extensively studied in theory as the building block of graphitic materials in other dimensions (*2*). For instance, it can be wrapped up into 0D fullerenes, rolled into 1D nanotubes, or stacked into 3D graphite [Figure 1.1(b)-(d)].

Well-isolated graphene as a 2D material was first discovered in 2004 by Andre Geim and Konstantin Novoselov at the University of Manchester (*3*), who were jointly awarded the 2010 Nobel Prize in Physics for this discovery. Using a remarkably simple Scotch tape method (Section 1.2), few- to mono- layer high-quality graphene sheets were deposited onto a Si wafer coated with 300 nm of SiO_2, and were readily identified under common white-light-illuminated optical microscopes. This simple preparation/detection process greatly facilitates studies of the material in various fields.

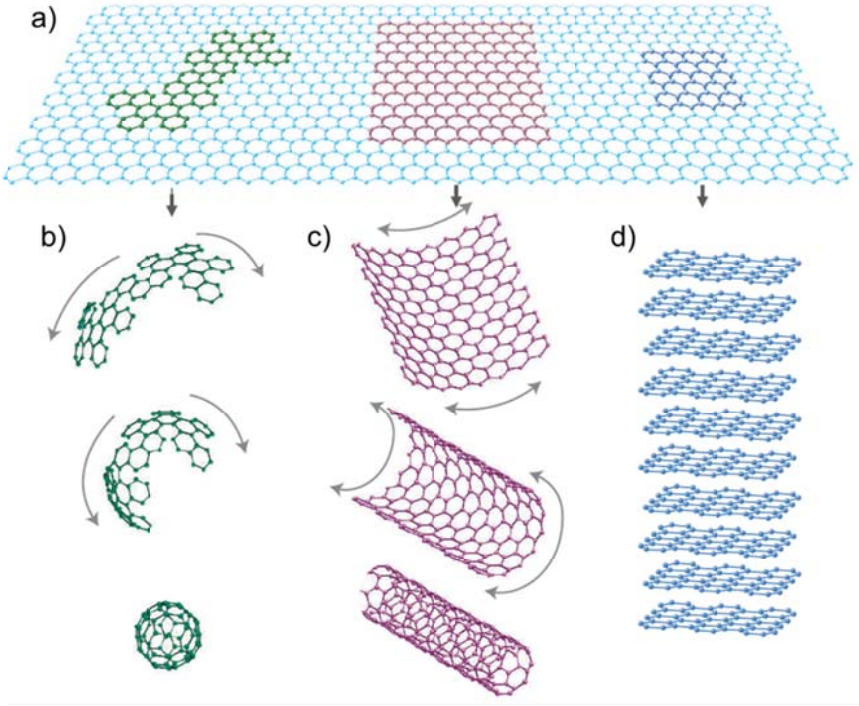

Figure 1.1: Graphene as the basis of all graphitic forms.
Graphene (a) can be wrapped to into fullerenes (b), rolled into nanotubes (c), and stacked into graphite (d). (*1*)

Indeed, the discovery of isolated graphene started a gold rush for graphene study. The material was found to have unique properties in various aspects, including but not limited to: high charge carrier mobility even at room temperature and relatively high charge carrier concentration (*4, 5*), a linear dispersion relationship with charge carriers mimicking massless relativistic particles (*6*), broadband uniform light absorption of 2.3% for single layer graphene (*7*), and exceptional mechanical strength (*8*) and thermal conductivity (*9-11*). Many potential applications have thus been proposed and realized for this material [see ref. (*12*) as a recent review].

Graphene is the main theme of my doctoral study. In the two research projects I will present in this dissertation, I studied the properties and applications of graphene in electrochemistry [Chapter 2, ref. (*13*)] and spintronics (Chapter 3), respectively. Now, before jumping into the research projects, I'd like to first introduce, in this chapter, some basic knowledge of graphene, electrochemistry, as well as magnetic tunnel junctions, which serves as the background information for the rest of this dissertation.

1.2 Different Ways to Prepare Graphene

Graphene can be prepared by many different methods. In this section, I will focus on discussing three major types of graphene that are closely related to my research described in this dissertation, i.e., graphene sheets that are derived from mechanical exfoliation, chemical vapor deposition, and liquid phase exfoliation.

1.2.1 Mechanically Exfoliated Graphene

Mechanically exfoliated graphene is obtained by peeling a monolayer of carbon atoms from bulk graphite. It is the type of graphene that was first discovered by Andre Geim and Konstantin Novoselov in 2004 (*3*), and its preparation process is remarkably simple.

In our lab, a layer of thin graphite flakes is spread over a Scotch tape surface by first attaching a Kish Graphite flake onto the tape surface and then repetitively pressing and peeling the original graphite flake at different spots of the tape. A second

Scotch tape is stuck to the first tape to peel off the top few layers of the graphite flakes. This tape is then attached to the target substrate. After gently pressing the tape with a pencil eraser for a couple of minutes, the tape is slowly removed from the target substrate. The Van der Waals force between the graphite and substrate will then make graphite flakes peel from its bulk part on the tape, leaving graphite flakes with various thicknesses on the substrate. Monolayer graphene flakes are then identified with optical microscopy by the contrast between the flakes and the substrate and later confirmed by Raman spectroscopy (Figure 1.2).

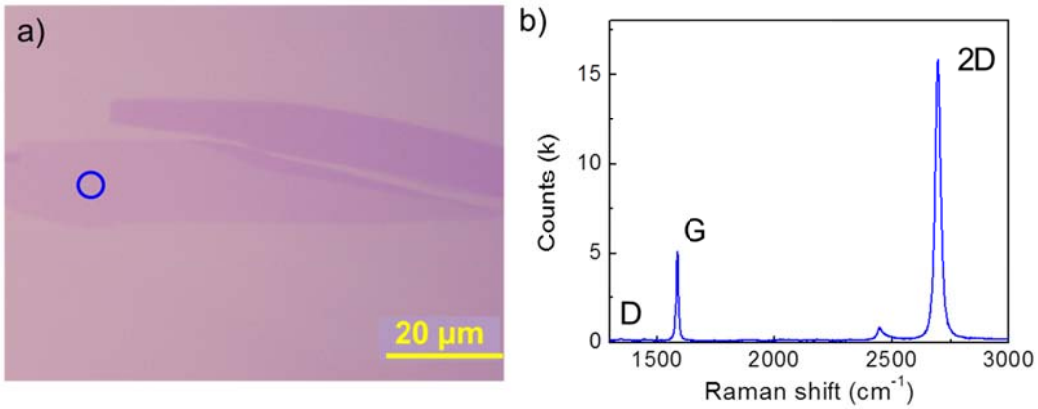

Figure 1.2: Monolayer graphene obtained from mechanical exfoliation
(a) Optical image of exfoliated graphene on a Si substrate coated with 300 nm oxide. (Scale bar: 20 μm) The Raman spectrum (b) obtained in the blue circle region confirms that the bottom flake is high-quality monolayer graphene: a significantly lower G peak than 2D peak and no observable D peak.

Mechanically exfoliated graphene is generally considered to be the most pristine form of graphene with the highest quality. For instance, the largest single-crystal graphene (> 1 mm) is prepared by mechanical exfoliation (*12*), and the highest room temperature mobility values achieved in graphene are measured with devices

fabricated from exfoliated graphene either suspended (*4*) or on hexagonal BN substrates (*14*). On the other hand, exfoliated graphene suffers from low production efficiency. Usually, only a few small pieces of graphene (10-50 μm in size) are randomly distributed on a centimeter-size substrate. It's time-consuming to locate the graphene flakes under an optical microscope for further processing. Exfoliated graphene is thus superb for scientific studies that require high quality graphene but faces difficulties in commercial applications which typically require mass production of the material.

As tips for increasing the yield and size of the exfoliated graphene, I found activating the Si/SiO_2 with oxygen plasma immediately before pressing down the tape with graphite flakes will significantly increase the yield of getting graphitic flakes and monolayer graphene on the substrate. In addition, graphene flakes deposited onto a freshly-cleaved mica surface in low humidity environments typically have much larger area than those on Si/SiO_2 substrates, presumably due to the large static charge interaction between graphene and the substrate.

1.2.2 Graphene Grown by Chemical Vapor Deposition on Copper Foils

Large-area monolayer graphene can be prepared by chemical vapor deposition (CVD) on copper foils/films (*15*). During growth, copper foils/films are exposed to a flow of a mixture of carbonaceous gas (CH_4 in our case) and H_2 at high temperature (~1000^{o}C). A continuous film of monolayer graphene forms on the copper surface during the cool-down process. The resultant graphene is then transferred from the

copper support to a dielectric surface with the help of a supporting PMMA layer for further usage (*15*).

CVD graphene on copper can be readily made in large sizes. Using a roll-to-roll technique, square meters of graphene have already been produced (*16*), and a computer-size touch screen has been made from this kind of graphene as a demonstration of potential applications (*16*). For scientific research, the large area of CVD graphene enables us to fabricate arrays of identical graphene devices with good control over the size, shape, and location of graphene. In contrast to exfoliated graphene, CVD graphene is intrinsically polycrystalline (*17, 18*) and generally has defects and contaminations caused by the graphene-transfer process. These factors may influence the overall quality of graphene. However, through optimizing the growth condition and careful handling of the material, the quality of CVD graphene is capable of approaching that of exfoliated graphene, especially over small length scales (*19-22*).

The CVD graphene sheets used for the studies presented in this dissertation were grown in furnaces either in Prof. McEuen's lab or at CNF (Cornell Nanoscale Science and Technology Facility). The procedure was modified from that developed by Ruoff *et al* (*15*), who first developed the technique. Figure 1.3 shows our CVD graphene after being transferred to a Si substrate coated with 300 nm oxide. The optical image and Raman spectrum indicate that the graphene is predominately monolayer [Figure 1.3(a) and inset]. An image from dark field transmission electron

microscopy (DF-TEM) indicates the CVD graphene has a polycrystalline structure with domain sizes of ~500 nm - 1μm [Figure 1.3(b)].

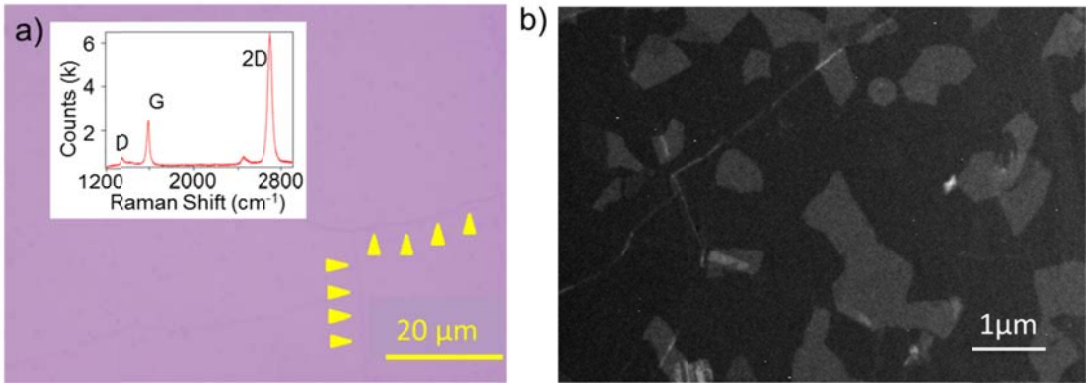

Figure 1.3: CVD graphene used in our studies

(a) Optical image of the CVD graphene on a Si chip coated with 300 nm oxide. The image shows uniform color suggesting uniform thickness of the graphene, while some occasionally discovered darker lines (indicated by the yellow triangles) correspond to wrinkles on graphene. Inset: The Raman spectrum of the CVD graphene, confirming that the graphene is a monolayer. (b) DF-TEM image of the graphene. The lightened regions define domains on graphene with the same lattice orientation.

1.2.3 Graphene Obtained by Liquid Phase Exfoliation or Graphene Oxide Reduction

Liquid-phase exfoliation (*23, 24*) of graphite is done by exposing the materials to solvents with surface tensions that favor an increase in the total area of graphite crystallites. The solvent used is typically non-aqueous, but aqueous solutions with surfactant can also be used. With the aid of sonication, graphite splits into individual

platelets and prolonged treatment yields a significant fraction of monolayer flakes in the suspension, which can be further enriched by centrifugation.

Another related method is the graphite oxide method (*25, 26*), in which graphite pellets are first oxidized and then ultrasonically exfoliated in an aqueous solution. After exfoliation of the graphene oxide suspension, the graphene oxide flakes can be (partially) reduced back to graphene.

These types of graphene are favored by the chemists. The graphene flakes are synthesized in a liquid bath and generally have a significant density of defects, which, in this case, can be an advantage for graphene functionalization. The flakes can also be deposited on different substrates either as pastes (*27-32*) or as a thin film when required (*33, 34*). Studies on these types of graphene focused on their applications in electrochemical sensing (*27-32*) and transparent conducting electrodes (*35-37*). However, they are not a good candidates to study the intrinsic properties of graphene because they are mixtures of graphene/graphite flakes with complex surface conditions (*38*), and that they have significantly lower mobility than exfoliated graphene and CVD graphene (*12*).

1.3 The Band Structure of Graphene: Linear Dispersion Relationship at the K/K' Points

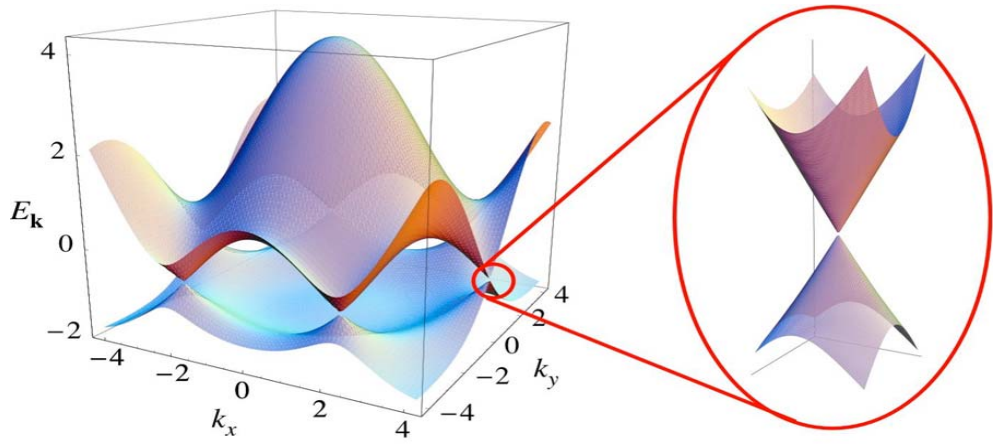

Figure 1.4: The band structure of graphene

Many unique properties of graphene come from its special band structure, which is characterized by the Dirac cone structures located at the K/K' points in its first Brilluoin zone. The Fermi-surface of undoped graphene is situated at the K/K' points. The doping level of graphene can be tuned by external gates or attached atoms/molecules; however, the Fermi-surface of graphene remains very close to the K/K' point, with charge carriers at the Fermi-surface following linear dispersion relationships determined by the Dirac cone structure:

$$E = \hbar v_F \sqrt{k_x^2 + k_y^2} \,. \qquad \text{Equation 1.1}$$

where $v_F = 10^6 \,\text{m/s}$ is the Fermi velocity of graphene.

1.4 Interactions between Graphene and Molecules: Previous Studies

While many unique properties are found in pristine graphene (section 1.1), it's also important to understand the interactions between graphene and its environment.

This is because graphene is a pure two-dimensional material that is fully comprised of surfaces: interactions from vicinal molecules can thus significantly change its properties. Indeed, it's found that addition of molecules onto the graphene surface can change the doping level (*39-41*) or even open band gaps in graphene (*42-44*). The latter case could convert graphene from a so-called "zero-gap semiconductor" to a real semiconductor, and facilitate potential application of graphene in logic circuits. Moreover, there is increasing interest in using graphene as an electrode material in different systems including graphene-based super capacitors (*45-47*), solar cells (*35, 37*), and electrochemical biosensors (*27-30*). Optimization of these applications requires a better understanding of the interactions between graphene as an electrode material and the related functional molecules.

Given the abovementioned importance of graphene-molecule interaction, several detecting techniques have been developed in previous studies, but each with its own limitations.

1.4.1 Raman Spectroscopy

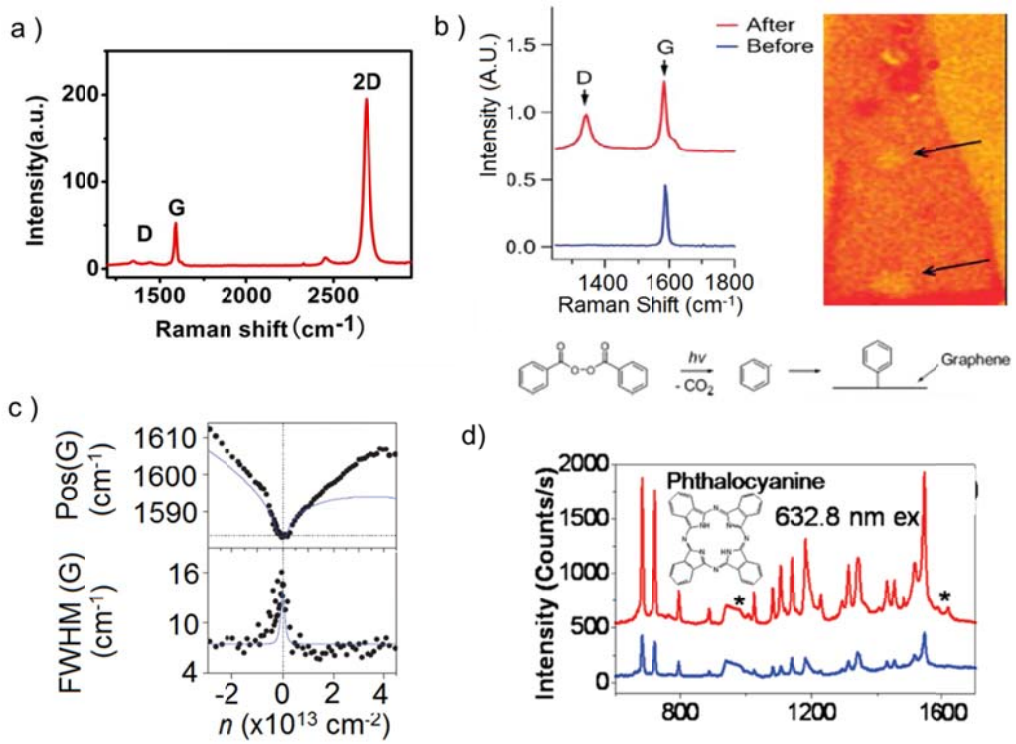

Figure 1.5: Detecting graphene-molecule interactions with Raman spectroscopy

(a) Typical Raman spectrum of graphene; (b) Example of using I_D/I_G to measure the degree of covalent functionalization. A pronounced D peak appears after phenyl groups are covalently bonded to graphene surface (*48*). (c) The position and FWHM as functions of the doping level of graphene (*49*). (d) Enhanced Raman spectrum with graphene substrate. red line and blue curves are respectively the Raman spectrum of phthalocyanine molecules on graphene and SiO_2 substrates (*50*).

Raman spectroscopy provides rich information about graphene. Figure 1.5 (a) shows the typical Raman spectrum of graphene. The three characteristic peaks are respectively the 2D peak (2700 cm^{-1}), G peak (1580 cm^{-1}), and D peak (1345 cm^{-1}). Among them, the D peak and G peak are particularly useful in detecting the graphene-molecule interactions in two different ways.

First, the ratio between the intensities of D peak and G peak (noted as I_D/I_G) are used to monitor the density of molecules that are covalently bonded to the graphene surface. I_D/I_G is typically an indicator of the ratio between sp^3 and sp^2 hybridized carbon atoms. While pristine graphene is entirely sp^2 carbon atoms, covalent bonding of molecules to the graphene surface converts sp^2 carbon to sp^3 carbon. We thus expect an increased I_D/I_G when the density of molecules that are covalently bonded to graphene increases [Figure 1.5 (b)].

Second, the position and stiffness of the G peak changes with the doping level of graphene [Figure 1.5 (c), (*49*)], and thus can be used to monitor the shift of the graphene doping level induced by attached molecules.

It's also possible to detect molecules on graphene by measuring the Raman spectrum of the molecules themselves. In particular, one study reported that graphene can serve as a substrate that enhances the Raman signal of molecules [Figure 1.5 (d), (*50*)], promising of more sensitive detection of molecules on the surface.

While being a handy method that can be conducted under ambient conditions, Raman spectroscopy only provides limited quantitative information, and changes in the Raman spectroscopy of graphene typically cannot be used to identify the molecular species that is interacting with graphene.

1.4.2 X-Ray Photoelectron Spectroscopy

When used to study the interaction between graphene and molecules, X-ray photoelectron spectroscopy (XPS) is distinguished from other techniques in that it

provides information on the chemical states of the system, e.g. the type of bonds formed between graphene and molecules. As an example, in ref (*51*), C-F, C-F_2 and C-F_3 bonds formed on the graphene surface after XeF_2 exposure are identified as individual peaks in XPS spectrum (Figure 1.6). In addition, the area underneath individual peaks can be used to quantitatively determine the amount of corresponding element/bonds on the graphene surface (Figure 1.6). With the abovementioned advantages, XPS measurement requires ultrahigh vacuum and extremely clean surfaces for characterization, thus limiting its application in characterizing graphene-molecule interactions.

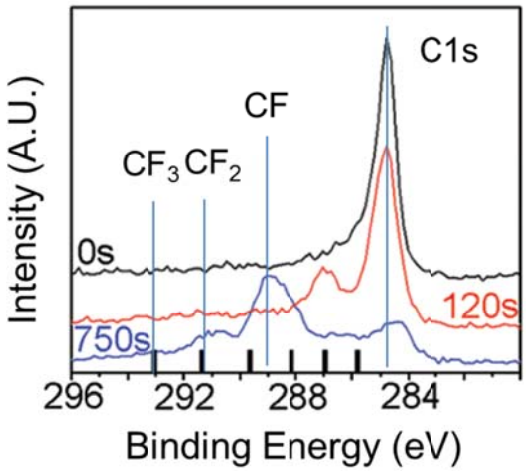

Figure 1.6: XPS of graphene fluorinated by XeF_2.

Black line: pristine graphene; Red line: graphene after exposure to XeF_2 for 120s; Blue line: graphene after exposure to XeF_2 for 750s. The C-F, C-F_2 and C-F_3 bonds formed on the graphene surface are identified as individual peaks in XPS spectrum. Quantitative analysis of the peak areas indicates the fractions of C-F,C-F_2, and C-F_3 is respectively 86%, 12% and 2% (*51*).

1.4.3 Scanning Tunneling Microscopy

Scanning tunneling microscopy (STM) enables direct visualization of molecules on graphene with atomic resolution. As an example, Figure 1.7 shows a STM image with a layer of self-assembled molecules on top of the graphene surface. While the possibility of directly seeing adsorbed molecules is certainly exciting, STM studies often require ultrahigh vacuum and are limited by very low throughput. It's also often difficult to identify the adsorbed molecular species with STM.

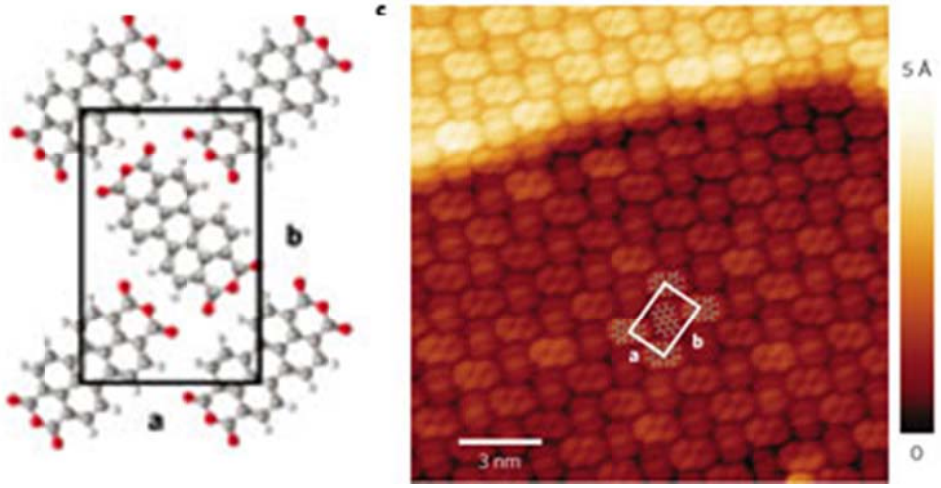

Figure 1.7: STM image of a self-assembled monolayer of perylene-3,4,9,10-tetracarboxylic dianhydride (PTCDA) molecules on graphene surface (*52*)

1.4.4 Transport Measurement

Transport measurements of graphene field effect transistors (FETs) detect graphene-molecule interactions by measuring the molecule-induced changes in the electrical properties of graphene, including changes in doping level, charge carrier mobility, or even an opened band-gap. One particular work suggested that graphene

FETs may be able to detect the desorption of individual NO_2 molecules from graphene surfaces [Figure 1.8, (*39*)]. On the other hand, it should be noted that graphene FETs only provide information on device resistivity, which may not always relate to graphene-molecule interactions.

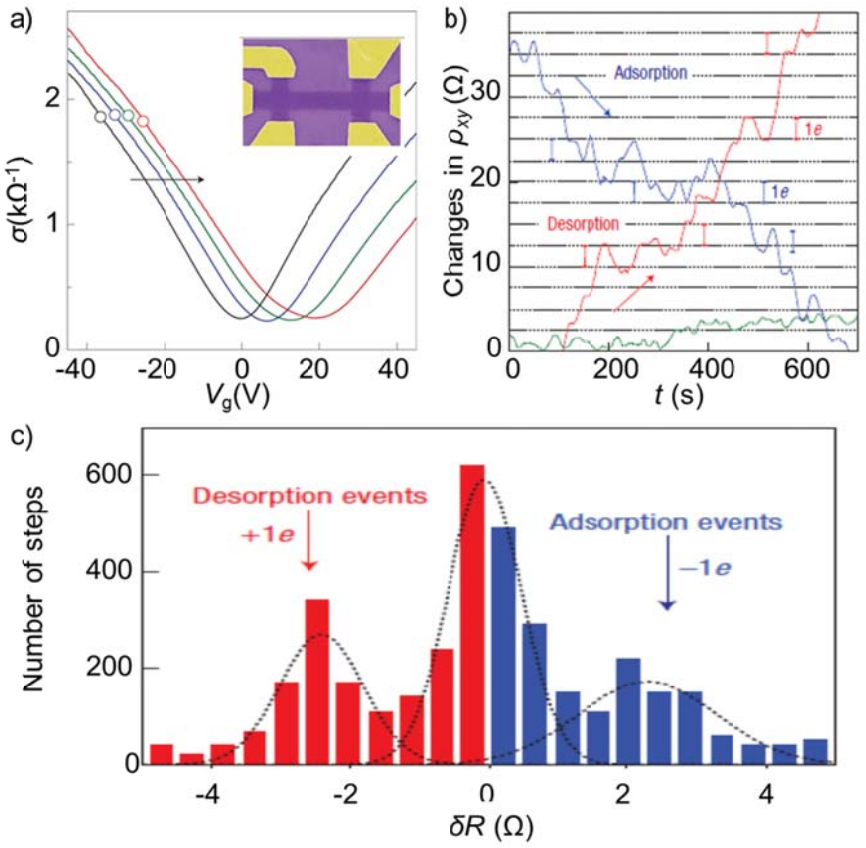

Figure 1.8: Graphene FET gas sensors may be capable of detecting individual gas molecules.

(a) Gate dependence of graphene resistivity. The neutrality point of graphene shifts higher at increased exposure to NO_2 molecules, indicating increased p-type doping of graphene induced by adsorbed molecules. Inset, false color scanning electron microscopy image of the graphene FET device. (b) Changes in the graphene Hall

resistivity as a function of time. Individual steps are ascribed to adsorption/desorption events of single NO_2 molecules. (c) Statistical distribution of the resistivity changes during the NO_2 desorption process. The two peaks appeared at +2/-2 Ω correspond to the detected adsorption/desorption events of individual NO_2 molecules (*39*).

1.5 Basics of Electrochemistry

The techniques discussed in Section 1.4 together have so far provided limited kinetic information about interactions between graphene and molecules. In comparison, electrochemistry is powerful for studying the kinetics of electron transfer between the electrode material and molecules. It also provides a quantitative approach to monitor adsorption and desorption of molecules from the electrode surface.

1.5.1 Heterogeneous Electron Transfer between an Electrode and Molecules

In electrochemistry experiments, the working, reference, and counter electrodes are inserted into the solution to construct an electrical circuit containing both electronic (electrodes and conducting wires) and ionic conductors (electrolytes containing the redox-active molecule of interest). A voltage is applied between the woking and reference electrodes to set the relative energy of electrons in the working electrode with respect to that of the molecular orbitals (MOs) of the molecules. Depending on the energy configuration, electrons in the molecules transfer either to or from the working electrode, accompanied by oxidization or reduction of the molecules at the electrode surface (Figure 1.9). This process is a heterogeneous reaction on the

electrode surface, as opposed to typical homogenous chemical reactions in the entire bulk solution.

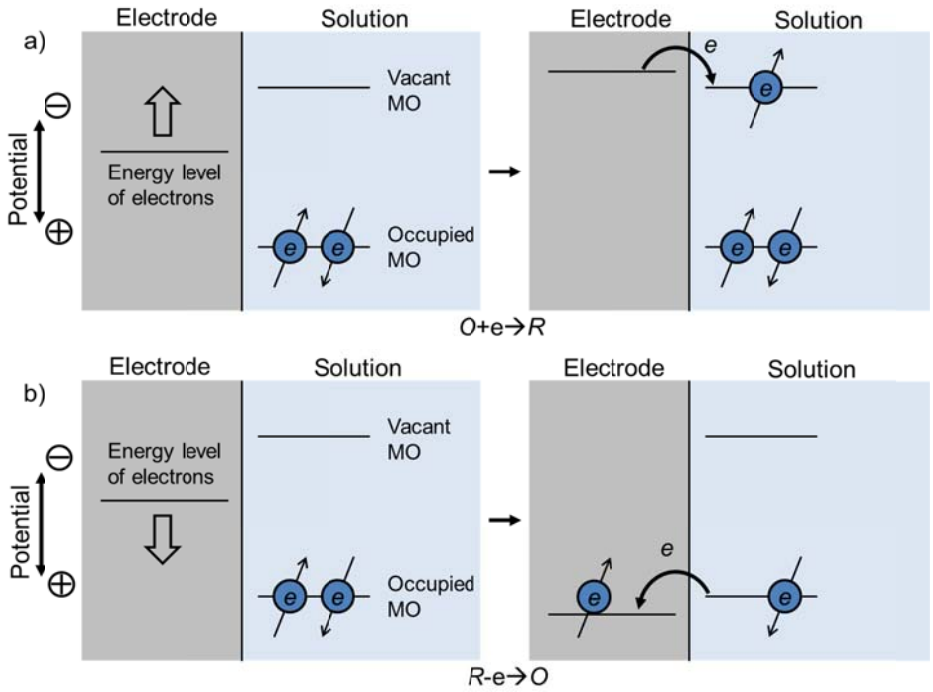

Figure 1.9: The energy configuration for heterogeneous reduction (a) and oxidation (b) processes.

Voltage applied to the working electrode changes the relative level of the energy of electrons in the electrode with respect to the highest occupied MO or lowest vacant MO. This causes electron transfer from (a) or to (b) the working electrode, with the molecules simultaneously being reduced or oxidized. (*53*)

The above heterogeneous electron transfer can be monitored by the Faradaic current (i_f) in the circuit, which is related with the rate of heterogeneous reaction by

$$\text{Rate}[\text{mol s}^{-1}\text{cm}^{-2}] = \frac{\mathrm{d}N}{\mathrm{d}t} = \frac{i_\mathrm{f}}{nA_{\mathrm{eff}}F}. \qquad \text{Equation 1.2}$$

in which n is the stoichiometric number of electrons consumed in the electrode redox reaction, F = 96,485 C/mol is the Faraday constant, and A_{eff} is the effective area (in cm^2) of the electrode. In addition to the Faradaic current, the so-called nonfaradaic current ($i_{\text{non-f}}$) is caused by charging/discharging of the electrical double-layer (EDL) at the electrode-solution interface, and is related to the double-layer capacitance (C_d) and potential scan rate (v) by,

$$i_{\text{non-f}} = C_\mathrm{d} v. \qquad \text{Equation 1.3}$$

In cyclic voltammetry (see Sections 1.5.3 and 1.5.4) measurements, the total current is the summation of faradaic and non-faradaic currents. When the faradaic current is of interest, the non-faradaic current should be subtracted. This is generally done by doing careful background subtraction, or reducing the potential scan rate (v).

1.5.2 Butler-Volmer Model of Heterogeneous Electron Transfer Kinetics

The Butler-Volmer model is widely used to understand the heterogeneous electron transfer kinetics between the working electrode and molecules. In this model, the rate of heterogeneous charge transfer is expressed in terms of two phenomenological parameters, which are respectively the standard rate constant (k^0) and transfer coefficient (α).

$$O + ne \underset{k_\mathrm{b}}{\overset{k_\mathrm{f}}{\rightleftarrows}} R. \qquad \text{Equation 1.4}$$

In a simple *n*-electron, one-step heterogeneous reaction (Equation 1.4), the rate constants for the forward (k_f) and backward reaction (k_b) at a certain electrode potential (E) are related to k^0 and α by (*53*):

$$k_f(E) = k^0 e^{-\alpha nF(E-E_0)/RT}$$
$$k_b(E) = k^0 e^{(1-\alpha)nF(E-E_0)/RT}, \quad \text{Equation 1.5}$$

in which R = 8.314 J mol^{-1} K^{-1} is the molar gas constant, T is temperature, F is the Faraday constant, and E_0 is the formal potential of the redox couple. Based on Equation 1.5, the complete current-potential characteristic of the heterogeneous reaction can be written as (*53*):

$$\begin{aligned} i_f &= AF\left(C_O(0,t)k_f - C_R(0,t)k_b\right) \\ &= AFk^0\left(C_O(0,t)e^{-\alpha nF(E-E_0)/RT} - C_R(0,t)e^{(1-\alpha)nF(E-E_0)/RT}\right) \end{aligned} \quad \text{Equation 1.6}$$

in which $C_O(0,t)$ and $C_R(0,t)$ are surface concentration of O and R species at time t.

The physical interpretation of the standard rate constant k^0 is that it measures the kinetic facility of the heterogeneous electron transfer between the electrode material and molecules (*53*). The actual value depends on both the type of electrode materials and the type of molecules. The largest measured standard rate constants are in the range of 100-200 cm/s while the smallest k^0 ever measured is lower than 10^{-9} cm/s (*53*).

The transfer coefficient α is a dimensionless number ranging from 0 to 1, and it measures the symmetry of the energy barrier between O and R in the reaction coordinate. α is equal to 0.5 for a symmetric barrier. In most systems, α turns out to lie

between 0.3 and 0.7, and it can usually be approximated by 0.5 in the absence of an actual measurement (*53*).

1.5.3 Investigating Electron Transfer Kinetics Using Cyclic Voltammetry

In cyclic voltammetric measurements, the voltage applied between the working and reference electrodes is scanned back and forth in a linear manner (Figure 1.10), while the resultant current is recorded. A plot of *current vs. working electrode potential* (cyclic voltammogram) is then generated and used for analysis. The shape of cyclic voltammogram is determined by both the heterogeneous electron transfer kinetics and the mass transport of molecules in the solution. Ultramicroelectrodes (UME) with lateral size smaller than ~25 μm shows completely different cyclic voltammograms than normal size electrodes under general voltage scan rate ($v = dE/dt$ ~1V/s), due to the greater mass transport rate at UME through radial diffusion. Different methods are thus developed to analyze the cyclicvoltammograms of UME and normal sized electrodes.

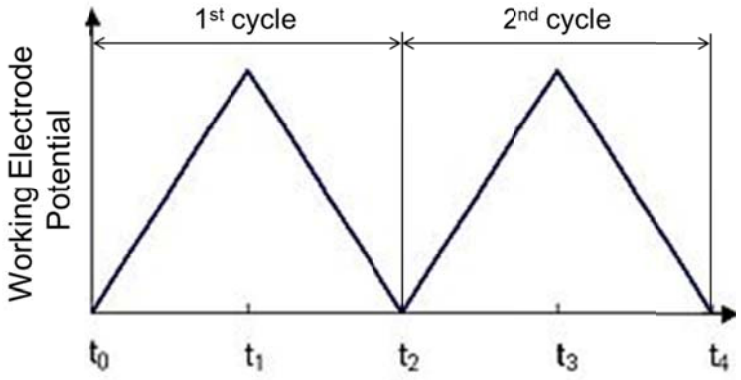

Figure 1.10: The voltage scan wave in cyclic voltammetry measurements.

Cyclic Voltammetry of Ultramicroelectrodes

The high mass transport rate at UMEs allows cyclic voltammetry to approach the steady-state regime, which is characterized by sigmoidal-shaped voltammograms (Figure 1.11). The current is limited at large over potentials due to mass transport limitations. For a disk-shaped ultramicroelectrode, the limiting current, also called steady-state current (i_{ss}), is scan-rate independent and is related to the effective area of the electrode (A_{eff}) by (*53*):

$$i_{ss} = \frac{4}{\sqrt{\pi}} nFDC_0^* A_{\text{eff}}^{1/2}. \qquad \text{Equation 1.7}$$

where D is the diffusion constant, and C_0^* is the bulk concentration of molecules in solution.

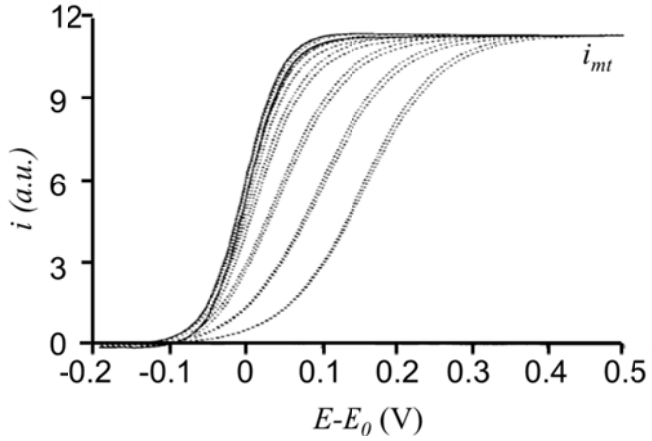

Figure 1.11: Steady-state cyclic voltammetry with ultramicroelectrode.
D =1×10^{-6} cm^{2}s^{-1} , r = 0.5 μm. The solid curves corresponds to k^0 > 100 cm/s, while the dashed curves from left to right correspond to cyclic voltammograms with k^0 = 1.1,

0.35, 0.11, 0.035, 0.011, 0.0035, and 0.0011 cm/s (*54*).

Kinetic parameters influence the rising part of cyclic voltammograms. As shown in Figure 1.11, the rising part of the cyclic voltammograms is shallower for systems with a smaller standard rate constant (k^0). Theoretically, the sigmoidal cyclic voltammogram should follow the Butler-Volmer equation(*53, 55*)

$$i_{\mathrm{BV}} = \frac{i_{\mathrm{ss}}}{1 + e^{-Fn(E-E_0')/RT} + K_0^{-1} e^{-Fn(1-\alpha)(E-E_0')/RT}} . \qquad \text{Equation 1.8}$$

Here K_0 is related to the standard reaction rate k^0 by:

$$K_0 = \frac{FA_{\mathrm{eff}} C_0^{*} k^0}{i_{\mathrm{ss}}} , \qquad \text{Equation 1.9}$$

It's thus possible to obtain the kinetic parameters by fitting the cyclic voltammograms to the Butler-Volmer equation.

The sigmoidal cyclic voltammetry has an upper detection limit for k^0. Above this limit, the process is diffusion-controlled (Nernstian case, solid curve in Figure 1.11), the slope of the rising part will approach a limiting value, and is no longer sensitive to changes in k^0. In this case, the lower bound of k^0 (noted as $k^0{}_{LB}$) can be estimated based on the size of the microelectrode (a as the radius) and diffusion constant (D) of the molecules following (*54*):

$$k^0{}_{LB} \approx \frac{80D}{\pi a} . \qquad \text{Equation 1.10}$$

Cyclic Voltammetry of Normal-Sized Electrodes

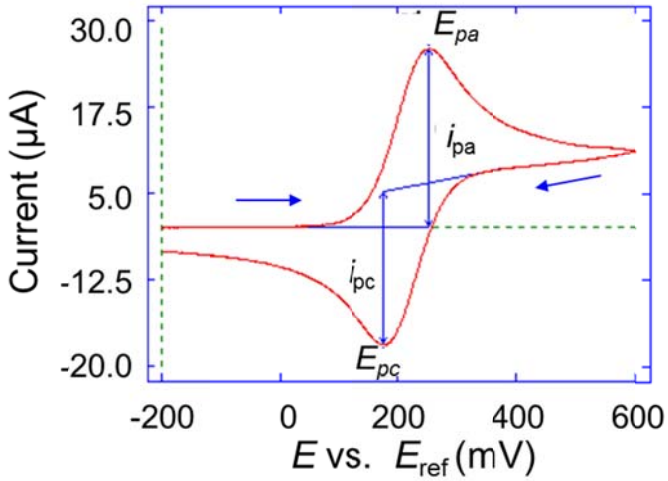

Figure 1.12: Peak-shaped cyclic voltammograms with a normal-sized electrode.

Typical cyclic voltammograms measured from normal-sized electrodes features an anodic [Figure 1.12, i_{pa} at E_{pa}] and a catholic peak [Figure 1.12, i_{pc} at E_{pc}] in the forward and backward scans, which respectively correspond to the oxidation and reduction of molecules.

Completely reversible cyclic voltammograms (Nernstian case) are measured in systems with high k^0 and under low potential scan rates, and they are characterized by a peak potential difference ($\Delta E_p \triangleq \left|E_{pa} - E_{pc}\right|$) of 59 mV, and a linear relationship between the peak current (i_{px}, x=a,c) and the square root of the potential scan rate ($v^{1/2}$) following the Randles-Sevcik equation (*53*):

$$i_{px} = 2.69\times10^5\ n^{3/2} A_{eff} D^{1/2} C_0^* v^{1/2}. \qquad \text{Equation 1.11}$$

Here, A_{eff}, C_0*, and D are respectively measured in cm^2, mol/cm^3, and cm/s.

Kinetic parameters can be extracted from quasi-reversible cyclic voltammograms, in which ΔE is greater than 59 mV and increases at higher potential scan rates and is not due to Ohmic drop in the cell. Specifically, the shape of quasi-reversible cyclic voltammograms are determined by a dimensionless parameter, ψ defined as (*53, 56*),

$$\psi = k^0 \sqrt{RT / \pi nDF} v^{-1/2} . \qquad \text{Equation 1.12}$$

Table 1.1 presents the value of ΔE_p for different ψ values. This value correspondence is broadly used [usually called the method of Nicholson (*56*)] to determine kinetic parameters from quasi-reversible cyclic voltammograms.

Table 1.1: Variation of ΔE with ψ (25°C) (*53*)

Ψ	ΔE (mV)
20	61
7	63
6	64
5	65
4	66
3	68
2	72
1	84
0.75	92
0.50	105
0.35	121
0.25	141
0.10	212

1.5.4 Detection of Molecule Adsorption and Desorption with Cyclic Voltammetry

In the experiments we have so far discussed, the molecules are dissolved in solution. Cyclic voltammetry is also capable of detecting the adsorption and desorption of redox active molecules. In this case the molecules are attached to the graphene surface.

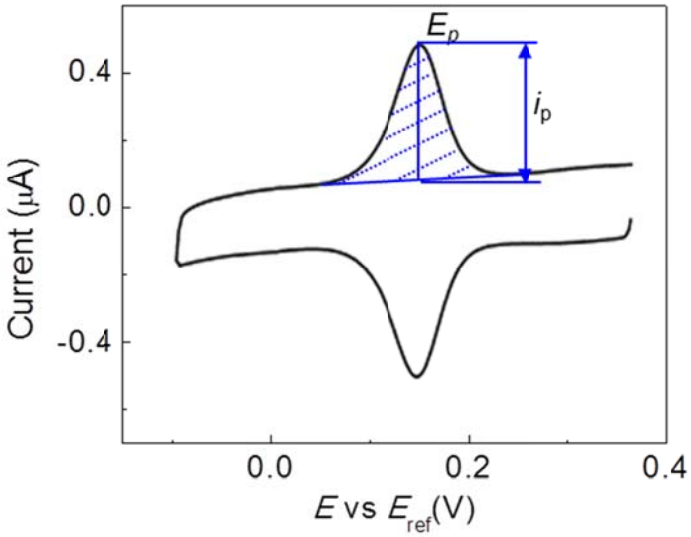

Figure 1.13: Typical cyclic voltammogram with molecules adsorbed on the electrode.

Figure 1.13 presents a typical cyclic voltammogram with redox active molecules being adsorbed on the electrode. Different from the diffusive cyclic voltammograms in which the anodic and catholic peaks are seperated by at least 59 mV (Section 1.5.3), the anodic and catholic peaks are now aligned at the same potential (E_p in Figure 1.13). In addition, the peak current (i_p in Figure 1.13) is proportional to the potential scan rate (v) rather than $v^{1/2}$ as in the diffusive cases. The

amount of molecules that are adsorbed on to the surface (Surface coverage, Γ) can be estimated from the area underneath the peaks (shadowed region in Figure 1.13) according to

$$S_{\mathrm{p}} = \int_{\mathrm{p}} i\mathrm{d}V = nvFA_{\mathrm{eff}}\Gamma \,. \qquad \text{Equation 1.13}$$

where Γ is the surface coverage of the molecule.

1.5.5 Three-Electrode Electrochemical Cell

A three-electrode configuration is generally used in electrochemical studies. Besides the working and reference electrodes, a counter electrode (typically made of Pt) is introduced to the electrochemistry measurement setup in this configuration. While the voltage is still applied across the working and reference electrode, the current is directed to flow through the counter electrode. This configuration allows the potential of the working electrode to be measured against a known reference electrode without compromising the stability of that reference electrode by passing current through it. Figure 1.14 shows the circuit for a three-electrode setup. It's usually carried out by a commercialized potentiostats, which in our case, is a CH Instrument Model 900 potentiostat.

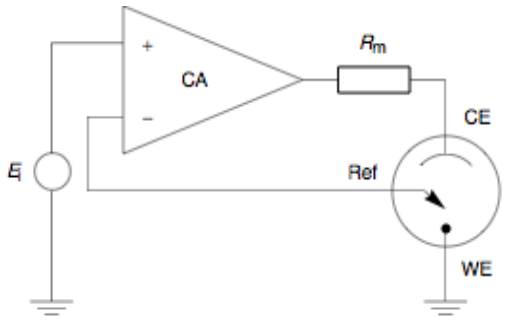

Figure 1.14: Schematic of the electrical circuit of a potentiostat,
Ref, CE, and WE represent reference, counter, and working electrodes respectively. The Current through the counter electrode is measured from the voltage drop across R_m.

1.6 Tunnel Magnetoresistance in Magnetic Tunnel Junctions

1.6.1 Tunnel Magnetoresistance Effect

The resistance of a magnetic tunnel junction (MTJ), which consists of a thin insulating layer (a tunnel barrier) sandwiched between two ferromagnetic metal (FM) layers (electrodes) depends on the relative magnetic alignment (parallel or antiparallel) of the electrodes. Typically, the tunneling resistance of the junctions is lower when the magnetization is parallel than when the magnetization is antiparallel, i.e., $R_P < R_{AP}$. This change in resistance with the relative orientation of the magnetic layers is called the tunnel magnetoresistance (TMR) effect, and is measured by the fractional change in resistance, which is called the magnetoresistance ratio, or magnetoresistance (*MR*) for short.

$$MR_{OPTIMISTIC} \equiv \frac{R_{AP} - R_P}{R_P} = \frac{G_P - G_{AP}}{G_{AP}} \qquad \text{Equation 1.14}$$

in an optimistic definition, and

$$MR_{\text{PESSIMISTIC}} \equiv \frac{R_{\text{AP}} - R_{\text{P}}}{R_{\text{AP}}} = \frac{G_{\text{P}} - G_{\text{AP}}}{G_{\text{P}}}. \qquad \text{Equation 1.15}$$

in a pessimistic definition. *MR* defined under one definition can be easily converted to the other.

The TMR effect was first observed in 1975 by Julliere who found that a Fe/GeO/Co MTJ exhibited a magnetoresistance ratio of 14% at 4.2 K (*57*). After 30 years of development, the highest achieved room-temperature magnetoresistance is now 604% in CoFeB/MgO/CoFeB magnetic tunnel junctions (MTJs) (*58*). This value goes up to 1144% at 5 K (*58*). This makes the TMR effect particularly important effect in the field of spintronics. MTJs are useful for practical applications, including spin-transfer-torque magnetic random-access memory (STT-MRAM) and hard drive disk read heads (*59-61*)

1.6.2 Resistance-Area Product of the Magnetic Tunnel Junctions

Besides the magnetoresistance, another important parameter for the magnetic tunnel junctions is the resistance-area product (*RA*). MTJs with low *RA* values are useful in many applications, including hard disk drive (HDD) read heads. The resistance of MTJs (*R*) must be kept low for good read head performance, because higher junction resistances result in higher Johnson and shot noise which degrades the signal-to-noise ratio, and further causes a longer *RC* time constant and thus a limited data rate. As the width of data track continues to decrease to enable more data tracks on the disk, the dimension of MTJ elements (*A*) need to be reduced accordingly and

thus their *RA* values must decrease. As a reference, *RA* values below 1 $\Omega.\mu m^2$ with a MR above 50% are required for recording densities beyond 200 $Gbit/in^2$ (*62*).

Lower *RA* value may be obtained by reducing the thickness of tunnel barrier. However, reducing the *RA* product to below a certain critical value usually yields a steep reduction in *MR (59)*. Great efforts have been made to obtain MTJs with both high *MR* and low *RA* by optimizing the barrier preparation process or exploring different barrier materials (*59, 62-69*). In the study presented in Chapter 3 of this dissertation, we explored the possibility of using graphene as a novel barrier material in magnetic junctions; the study indicates that graphene-based MTJs are tunnel junctions with low *RA* products and moderate *MR*.

CHAPTER 2

ELECTROCHEMISTRY OF INDIVIDUAL MONOLAYER GRAPHENE SHEETS

2.1 Introduction

As discussed in Chapter 1 (section 1.4), while it's very important to understand the interaction between graphene and molecules, commonly used techniques provide limited information on the electron transfer kinetics between graphene and molecules.

Electrochemistry provides a means to measure electron transfer kinetics and interactions between molecules and electrode surfaces [Section 1.5, (*53, 70, 71*)]. Carbon materials in various forms have been extensively used as electrodes in both academic studies and industrial applications (*72*). In particular, electrochemical studies on novel forms of carbon materials, including carbon nanotubes (*55, 73*), fullerene films (*74*), and doped diamond (*75, 76*), have revealed rich surface chemistry. Prior to our study, electrochemical studies on chemically synthesized graphene pastes (Section 1.2.3) suggested graphene may have favorable electron-transfer kinetics (*27-32*). However, those studies were restricted to powders of synthesized graphene flakes pasted on Pt or glassy carbon electrodes, and questions abound as to whether the improved electron transfer kinetics simply reflect increased microscopic surface areas (*38*). The electrochemistry of monolayer graphene sheets has not been reported due to the apparent difficulties in device fabrication.

In this chapter, I present our fabrication and study of devices in which a well-defined area of single-layer graphene served as the working electrode in electrochemical experiments (*13*). We examined both mechanically exfoliated and chemical vapor deposited (CVD) graphene, with a focus on investigating the interactions between graphene and the simple redox molecule ferrocenemethanol (FcMeOH). These studies were done in close collaboration with Dr. Cen Tan in Prof. Abruña's group in the Chemistry Department at Cornell. To our knowledge, we are among the first groups who conducted electrochemical studies on individual pieces of graphene sheets.

2.2 Working Electrodes Made of Individual Graphene Sheets for Electrochemical Measurements

2.2.1 Structure and Fabrication Processes of the Graphene Working Electrode

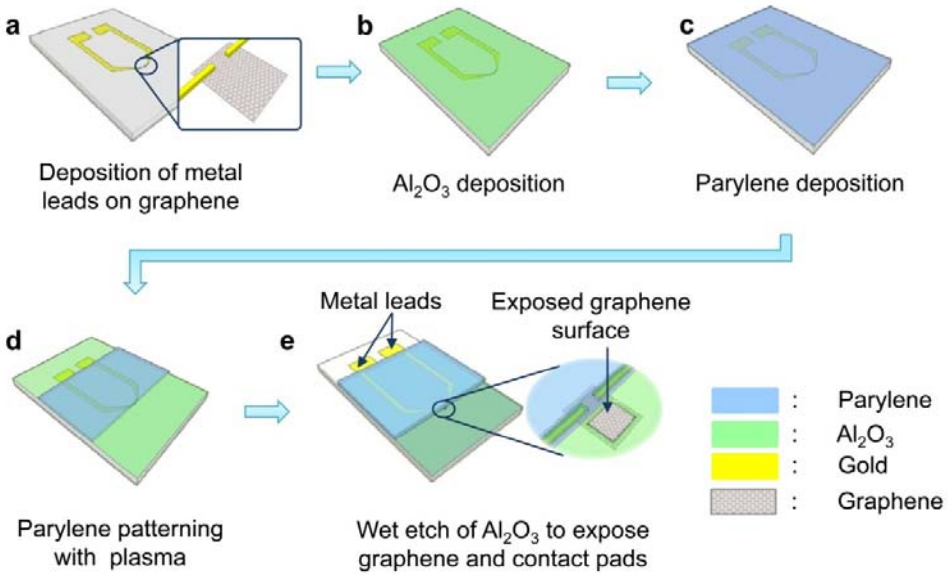

Figure 2.1: Procedure for fabricating monolayer graphene sheets into working

electrodes for electrochemical characterization.

Figure 2.1 illustrates our fabrication scheme of graphene working electrodes. A monolayer graphene sheet was first deposited on a Si substrate coated with 300 nm oxide. As noted above, two types of graphene were investigated, namely, mechanically exfoliated graphene extracted from Kish graphite flakes [Section 1.2.1, (*77*)] and CVD graphene that's grown on copper foils and then transferred onto SiO_2 [Section 1.2.2, (*15*)]. For both types of graphene, photolithography was employed to connect each piece of graphene with at least two metal leads Figure 2.1 (a)]. A resistance of ~1 kΩ is typically found in two-point measurements between the leads, indicating good contacts to graphene (*78, 79*). A 100 nm Al_2O_3 layer Figure 2.1 (b)], followed by a 600 nm parylene layer Figure 2.1 (c)] were deposited on top of the metal leads to fully isolate them from the solution in electrochemistry experiments. Oxygen plasma was employed to remove a region of the parylene layer above graphene while keeping the metal leads covered Figure 2.1 (d)]. Finally, a window through the Al_2O_3 layer was made using wet etch to expose a well-defined area of the graphene surface Figure 2.1 (e)]

This design ensures that graphene is the only electrochemically active surface that is in contact with the solution during electrochemical measurements. The sizes of the exposed graphene surfaces ranged from ~15×15 μm^2 for mechanically exfoliated graphene to ~0.38×0.50 mm^2 for CVD graphene [note CVD graphene can be formed in much larger sheets than exfoliated graphene (Section 1.2)]. In the final step,

vacuum annealing at 350 ^{o}C was used to remove organic residuals on the graphene surface.

2.2.2 Characterizations of the Graphene Electrodes with Raman Spectroscopy and Atomic Force Microscopy

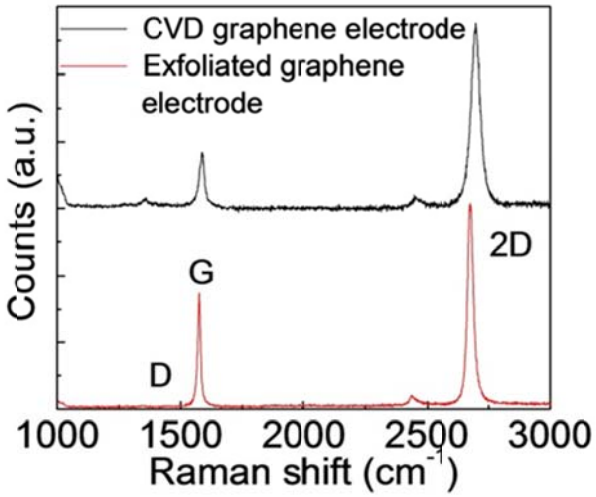

Figure 2.2: Raman Spectra of the graphene working electrodes after the fabrication process is complete.

The spectrum backgrounds are almost zero for both types of graphene. The Spectrum for CVD graphene is shifted up for clarity.

The fabricated graphene electrodes were characterized using multiple methods to confirm the quality and cleanliness of the graphene surface. Figure 2.2 shows the micro Raman spectra of the graphene working electrodes after the device fabrication process was completed. For both types of graphene, a symmetric single peak is observed for the 2D band, with a peak intensity that is significantly higher than the G peak. These results indicate that the graphene electrodes investigated in this study are monolayer graphene sheets (*80*). For electrodes made of mechanically exfoliated graphene, no observable D peak is found at ~1350 cm^{-1}, indicating that the graphene

sheet is clean and effectively defect-free. In comparison, a small D peak is observed for electrodes made of CVD graphene, indicating a less pristine layer as is generally the case for such samples (*16, 22, 81*).

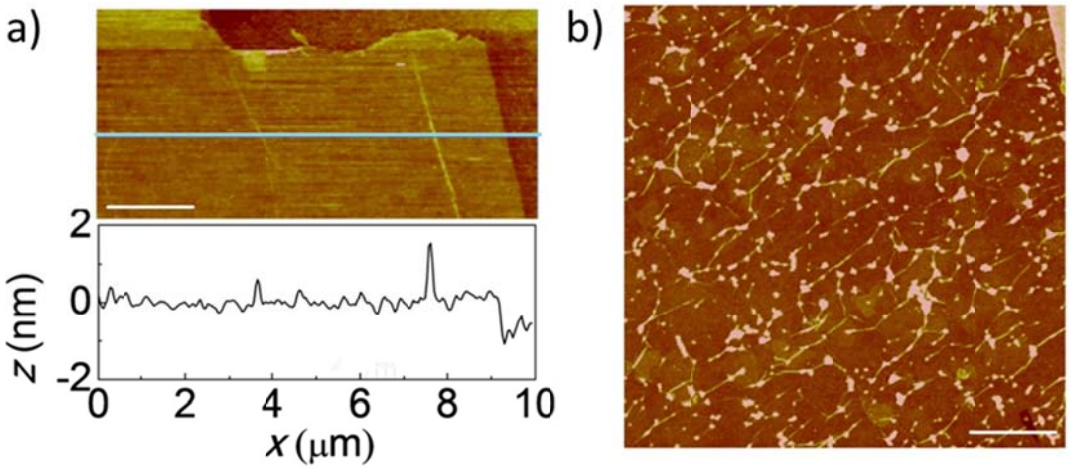

Figure 2.3: Atomic force microscope images of the graphene working electrodes after the fabrication process is complete.
(a) Exfoliated graphene electrodes. A cross-sectional profile is given for the blue line; (b) CVD graphene electrodes. Scale bars: 2 μm

Atomic force microscope (AFM) images of the devices further supported these observations. Dust- and dirt-free surfaces (rms roughness ~180 pm away from the large wrinkles) were observed for electrodes made of exfoliated graphene sheets [Figure 2.3(a)]. The step height of the graphene with respect to SiO_2 is ~0.8 nm, in excellent agreement with the known value for pristine graphene (0.5 to 1 nm) (*3*). In comparison, electrodes made of CVD graphene sheets were more disordered: features including larger wrinkles, particulates, and domain-like structures were observed following the CVD growth and transfer process [Figure 2.3(b)]. This result is in agreement with previous studies (*15*).

2.3 Measurement Setups for Electrochemical Studies

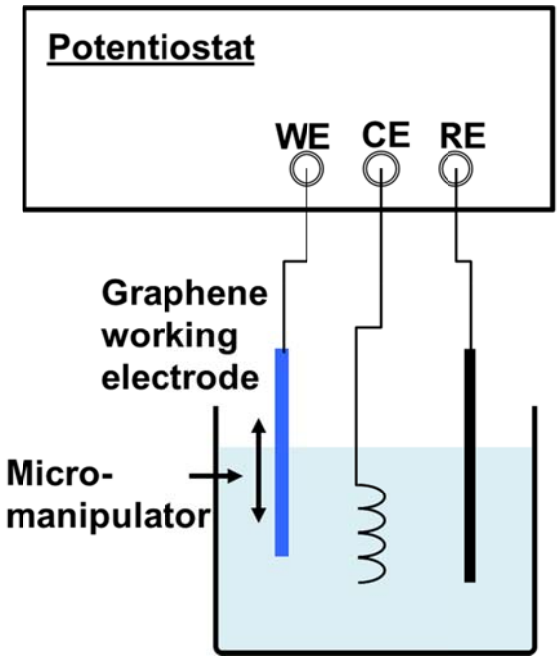

Figure 2.4: The measurement setup used in our study.

Figure 2.4 illustrates the measurement setup we used to investigate electrochemistry on graphene electrodes. Cyclic voltammograms were measured in a three-electrode configuration (Section 1.5.5) using a CH Instrument Model 900 potentiostat. The fabricated graphene electrode was used as the working electrode. An Ag/AgCl electrode (saturated KCl) and a Pt wire were used as the reference and counter electrodes, respectively. During measurement, a micromanipulator was used to smoothly insert the graphene electrode into the solution. The cell was placed in a Faraday cage on top of an optical table to reduce electronic and acoustic noise. The noise level of our experiments was found to be ~0.02 nA when measuring ~10 nA current with our exfoliated graphene electrodes.

2.4 Results from Electrochemical Measurements

2.4.1 Cyclic Voltammetric Study with Mechanically Exfoliated Graphene Electrodes

Figure 2.5 shows the cyclic voltammograms measured using an exfoliated graphene electrode in FcMeOH solution at different scan rates. FcMeOH was chosen for our studies for its simple redox behavior (one-electron outer-sphere process) and good chemical stability in an aerobic aqueous environment. We observed sigmoidal voltammograms and scan-rate-independent limiting steady-state currents, both characteristic of radial diffusion on ultramicroelectrodes (Section 1.5.3). This is in agreement with the electrode area, which had lateral dimensions smaller than the characteristic length used to define an ultramicroelectrode [~25 μm, (*53*)].

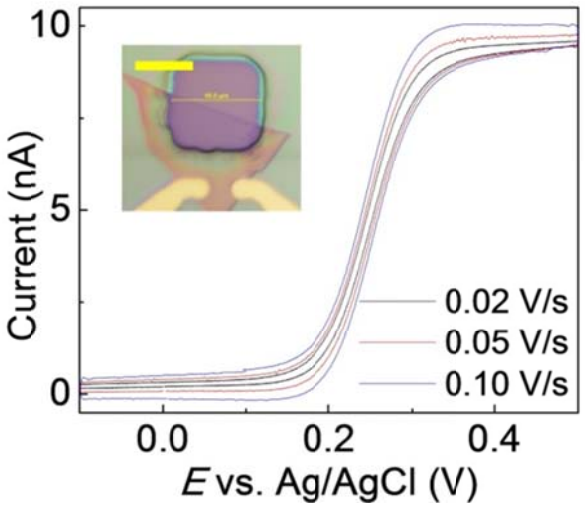

Figure 2.5: Cyclic voltammograms measured with a mechanically exfoliated graphene electrode.

Measured in FcMeOH (5.2 mM) in H_2O/ 1M KCl solution at different potential scan rates. Inset: optical image of the graphene electrode. Scale bar: 10 μm.

The slight hysteresis in the forward and reverse scans was due to the capacitance of the measurement system, and became more significant at larger voltage scan rates. In the following discussion, we thus use the cyclic voltammograms measured at the slowest scan rate for our analysis and carefully subtracted the background to eliminate the influence of the capacitance.

Modeling the electrode as a disk-shaped ultramicroelectrode (*53*), the effective area (A_{eff}) of an ultramicroelectrode is related to the steady state current (i_{ss}) by

$$A_{\text{eff}} = \pi \left(\frac{i_{\text{ss}}}{4nFDC_0^*} \right)^2 . \qquad \text{Equation 2.1}$$

where C_0*=5.2 mM is the FcMeOH concentration, $D = 7.4\times10^{-6}$ cm^2/s is the diffusion constant of FcMeOH, $n = 1$ is the number of electrons involved in the redox reaction, and F is the Faraday constant. From the experimental i_{ss} (9.01 nA), we therefore calculated the effective area of this graphene electrode to be 117±8 μm^2. This result is in good agreement with the geometric area we measured from the AFM image (130 μm^2), and provides evidence that the redox reaction occurs on a relatively clean graphene surface. Significant contamination, especially by irreversibly adsorbed species on the graphene surface, would lower the A_{eff} (although this measurement may not be sensitive to non-uniform small contaminants scattered across the surface). Conversely, any current leakage would drastically increase the calculated A_{eff}.

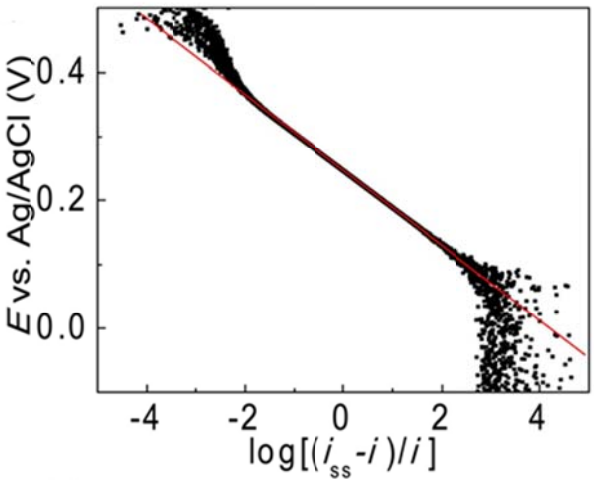

Figure 2.6: Plot of *E vs* log[(i_{ss}-*i*)/*i*] with the experimental cyclic voltammogram data acquired at a potential scan rate of 0.02 V/s in Figure 2.5. Forward scan and after background subtraction. The red line is a linear fit to the data.

The ultramicroelectrode geometry allows fast reaction kinetics to be measured using voltammetry (*53, 71*). A plot of *E* vs. log[(i_{ss}-*i*)/*i*], where *i* corresponds to the current measured at an applied potential *E,* is commonly used to characterize the reversibility of the kinetics for ultramicroelectrodes. For a reversible one-electron transfer reaction in which the reaction rate is much greater than the rate of mass transport, this plot should be linear with a slope of 59 mV (*53*). As the reaction rate is reduced relative to the mass transport rate, the slope increases. Figure 2.5 (b) presents a plot of *E* vs. log[(i_{ss}-*i*)/*i*] using the v = 0.02 V/s cyclic voltammogram data in Figure 2.5. As is evident from the figure, good linearity was achieved and the slope was 58.3±0.3 mV, from which we conclude that the heterogeneous reaction rate of FcMeOH at the graphene surface is much greater than the mass transport rate.

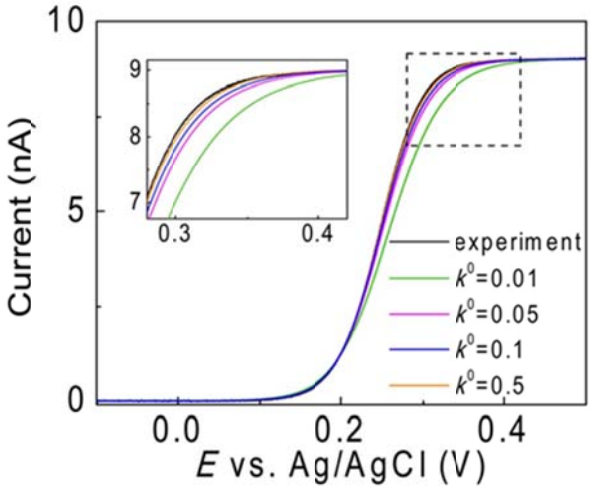

Figure 2.7: Fit of the Butler-Volmer kinetics (Equation 2.2) to the experimental voltamogram (scan rate = 0.02 V/s in Figure 2.5) for different k^0 values.

Inset: Close-up view of the dashed square region in the main figure.

We can estimate a lower limit for the standard heterogeneous charge transfer rate constant k^0 by fitting the experimental voltammograms to the Butler-Volmer model (Section 1.5.3), in which the oxidative current for a one step, one electron process is (*53*):

$$i_{BV} = \frac{i_{ss}}{1 + e^{-F(E-E_0')/RT} + \left(\frac{FA_{eff}C_0^*}{i_{ss}}k^0\right)^{-1} e^{-F(1-\alpha)(E-E_0')/RT}}. \qquad \text{Equation 2.2}$$

where R is the molar gas constant, T is the absolute temperature, E is the applied potential, E_0' is the formal potential of the redox couple, and α is the transfer coefficient. Figure 2.5(c) shows the best fits of Equation 2.2 to the experimental data with different fixed k^0 values. E_0' and α are used as fitting parameters, with α being confined to be between 0.3 to 0.7 and i_{ss} fixed to be 9.01 nA. The fitting quality

increases monotonically as the k^0 value increases. Satisfactory fits are obtained for k^0 greater than 0.5 cm/s. We thus estimate the lower limit of k^0 at the mechanically exfoliated graphene electrode to be 0.5 cm/s. Simple estimations based on the observation that the ultramicroelectrode voltammogram is reversible also gave similar lower bounds of k^0 of 0.2-0.6 cm/s (*53, 82*).

2.4.2 Cyclic Voltammetric Study with CVD Graphene Electrodes

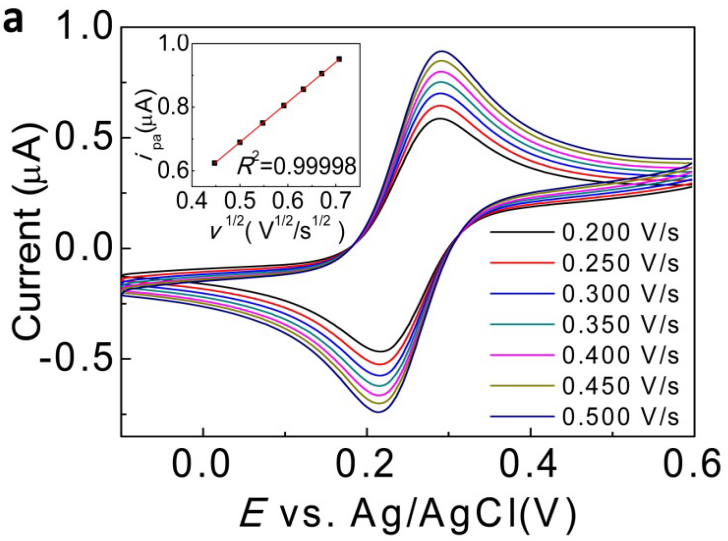

Figure 2.8: Cyclic voltammograms measured with a CVD graphene electrode. Measured in FcMeOH (1 mM) in H_2O/ 0.1M KCl solution at different potential scan rates. Inset: The peak current extracted from the cycic voltammograms presented in the main panel as a function of the square root of scan rate ($v^{1/2}$)

Figure 2.8 shows the cyclic voltammograms measured at a CVD-grown graphene electrode in FeMeOH solution at different scan rates. Peak-shaped voltammograms were observed, as expected, given the large area (0.19 mm^2) of the CVD graphene working electrode. Due to the significant currents (~1 μA) in this

measurement, for detailed analysis, we should correct for the effects of uncompensated resistance (*53*). Given the three-electrode measurement configuration and the high concentration of supporting electrolyte (0.1 M KCl) in the solution, the resistance from the solution is negligible. The major source of resistance comes from the contact resistance between the metal leads and the graphene sheet, which is ~1100 Ω for the device presented in the Figure 2.8. We performed the resistance correction (see Appendix, Section 2.7.1), and the resulting peak currents (i_p) are plotted in the inset of Figure 2.8 as a function of the square root of the scan rate ($v^{1/2}$). A highly linear dependence is observed.

Using the Randle-Sevcik equation [Equation 1.11, Section 1.5.3], the effective surface of the working electrode was estimated to be 0.172±0.006 mm^2. This value, similar to the case of exfoliated graphene electrode, is in good agreement with the geometric area of this electrode (designed to be 0.19 mm^2), indicating that the redox reactions occur predominantly on a clean graphene surface.

Kinetic parameters for the reaction of FcMeOH with CVD graphene can be measured from the potential difference between the oxidation and reduction peaks (ΔE_p) as a function of the scan rate. As shown in Figure 2.9, ΔE_p (after proper resistance correction; see Appendix, Section 2.7.1) ranges from 68.6 to 72.6 mV and increases at higher scan rate, indicative of quasi-reversible kinetics in the system. Following the method of Nicholson (*53, 70*) (Table 1.1; see also discussions in Section 1.5.3), these ΔE_p values can be converted into a dimensionless kinetic

parameter ψ that is directly proportional to the reciprocal of the square root of scan rate, $v^{-1/2}$:

$$\psi = k^0 \sqrt{RT / (\pi nFD)}\ v^{-1/2}. \qquad \text{Equation 2.3}$$

The standard rate constant k^0 can thus be determined from a linear fit to the ψ-$v^{-1/2}$ relationship (Figure 2.9, red curve). From the slope we find k^0 to be 0.042 ± 0.002 cm/s. To make sure that the relatively high k^0 value we obtained on the CVD graphene electrode is not an artifact resulting from overcorrection of resistance, we have also calculated k^0 without resistance correction (Appendix, Section 2.7.1). A k^0 value of 0.037 cm/s was determined, which is ~90 % of the k^0 (0.042 cm/s) obtained with resistance correction, indicating that the resistance correction only has a minor effect on the final k^0 value.

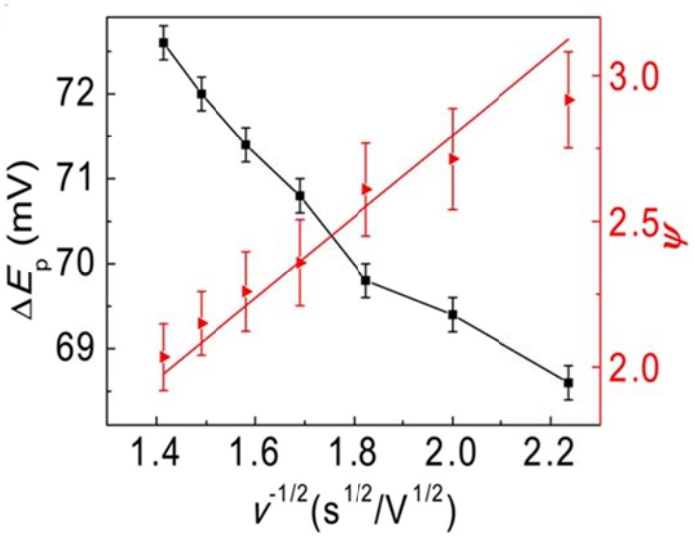

Figure 2.9: Peak separation and Nicholson's kinetic parameter versus the reciprocal of the square root of the potential scan rate.
A linear fit is used to determine the standard heterogeneous charge transfer rate

constant (k^0).

2.4.3 Fast Heterogeneous Electron Transfer Kinetics on Graphene

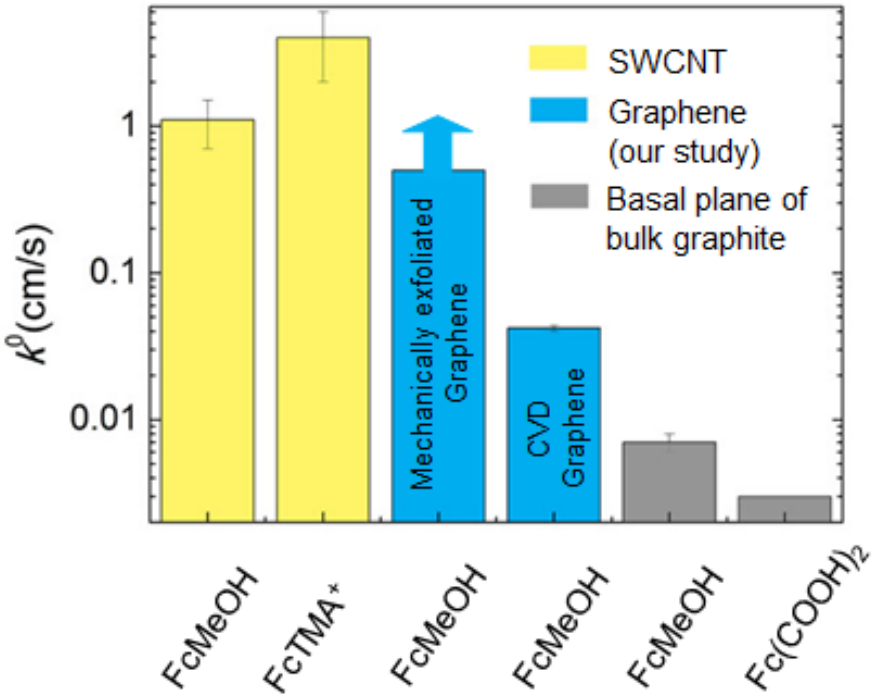

Figure 2.10: Comparison of k^0 of ferrocene derivatives at SWCNT, graphene surfaces, and the basal plane of bulk graphite.
FcMeOH on SWCNT: (*83*); FcTMA$^+$on SWCNT: (*72*); FcMeOH on HOPG: Our control measurement (Section 2.7.2); Fc $(COOH)_2$ on HOPG: (*84, 85*).

We now compare the k^0 values we measured on graphene surfaces to those from other types of sp^2 carbon surfaces. Using experimental and analysis methods similar to those described for the CVD graphene electrode, we found the k^0 value of FcMeOH at the basal plane of a freshly prepared bulk graphite electrode to be 0.007 cm/s (Appendix, Section 2.7.2). k^0 for a similar ferrocene derivative, ferrocenedicarboxylic acid [$Fc(COOH)_2$], at the graphite basal plane has been reported to be 0.003 cm/s (*84, 85*). These values are about one order of magnitude smaller than

the k^0 we measured at the CVD graphene electrode (0.042 cm/s), and two orders of magnitude smaller than the k^0 we measured on mechanically exfoliated graphene (>~0.5 cm/s). However, even larger values of k^0 have been measured for ferrocene derivatives at single wall carbon nanotubes (SWCNTs), which can be regarded as wrapped graphene sheets: for FcMeOH on SWCNTs, k^0 = 1.1 ± 0.4 cm/s (*83*), and for ferrocenylmethyl-trimethylammonium ($FcTMA^+$) on SWCNTs k^0 = 4 ± 2 cm/s (*72*). Figure 2.10 displays the abovementioned k^0 values on a logarithmic scale.

Earlier studies on graphene pastes have also suggested that graphene may have favorable electron transfer kinetics when compared to graphite (*27-30, 32*). The enhanced k^0 is likely related to the observations that graphene (and SWCNTs) have dramatically enhanced chemical reactivity when compared to the basal plane of bulk graphite (*43, 86, 87*). This enhancement was generally believed to be a consequence of the large intrinsic corrugations (*88, 89*) of graphene sheets that are not present in the atomically flat surfaces of bulk graphite. The corrugations lead to considerable curvature and strain in graphene sheets at the atomic scale, which, in turn, activate the graphene surface towards chemical reactions (*43, 87*). In the meantime, theoretical and experimental studies have further indicated that the corrugations in graphene sheets may also create local midgap states (*90, 91*), which we believe might further contribute to the enhancement of k^0. When compared with exfoliated graphene, the relatively smaller k^0 of CVD graphene may be related to its lower electron mobility.

2.4.4 Detection of Molecule Adsorption and Desorption on Graphene

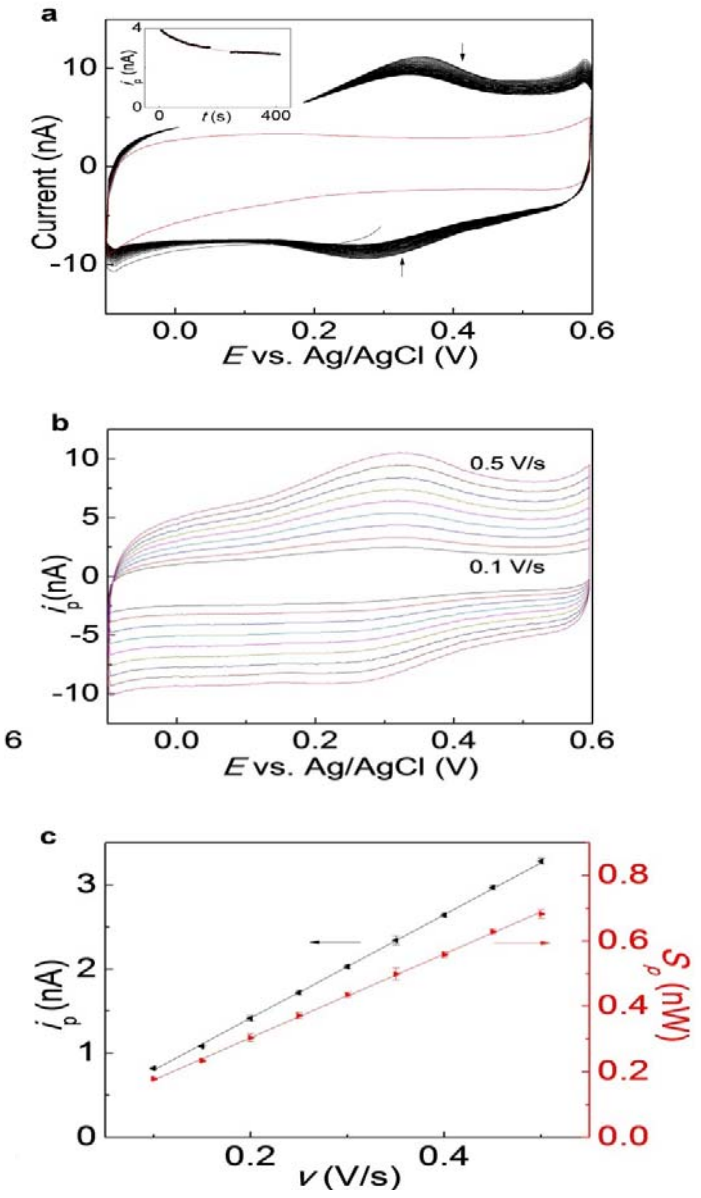

Figure 2.11: Real-time electrochemical detection of desorption of FcMeOH from graphene surfaces.

(a) Black line: cyclic voltammograms measured on a CVD graphene electrode in 0.1 M KCl solution, after adsorption of FcMeOH on the graphene surface. Gradual desorption of FcMeOH is observed. The scan rate is 0.4 V/s. Red line: background

voltammogram of a control electrode made from the same graphene sheet without FcMeOH adsorption. Inset: decrease of the anodic current peak (i_p) as a function of time. (b) Cyclic voltammograms measured at different scan rates after the desorption process reached equilibrium. Curves from black to pink represent cyclic voltammograms measured at 0.1, 0.15, 0.2, 0.25, 0.3, 0.35, 0.4, 0.45, and 0.5 V/s, respectively. (c) Plot of the anodic peak current (i_p) and peak area (S_p) versus the scan rate (v).

We have also demonstrated that electrochemistry measurement is capable of detecting molecule adsorption and desorption on graphene in real-time. After voltammetric measurements using CVD graphene in 1 mM FcMeOH for ~15 min, we rinsed the graphene electrode thoroughly with deionized water and placed it in 0.1 M KCl solution with no added FcMeOH. Figure 2.11 (a) shows the cyclic voltammograms subsequently measured. We observed oxidation and reduction peaks at potentials similar to those seen in the diffusive voltammograms recorded in FcMeOH solution [Figure 2.11 (a)]. However, the current levels were more than two orders of magnitude lower. These peaks were not present in the voltammograms of control CVD graphene electrodes that had not been previously exposed to FcMeOH in pure electrolyte solution without added FcMeOH [Figure 2.11 (a)]. We conclude that the signals arise from FcMeOH molecules adsorbed onto the CVD graphene surface. In addition, the amplitudes of these peaks decreased during continuous cyclic voltammetric scans on a time scale of ~100 s, and tended to stabilize to finite values after ~5 min [Figure 2.11(a), inset], indicating that a fraction of the adsorbed FcMeOH molecules gradually desorb from the surface (likely due to weak adsorption) but some electrochemically active, irreversibly adsorbed molecules remain.

Figure 2.11(b) shows cyclic voltammograms measured at different scan rates after the desorption process had reached a steady state. The peak separations (ΔE_p) at different scan rates ranged from 40 mV to 54 mV, significantly smaller than the ΔE_p value of diffusive cyclic voltammograms (59 mV), providing additional evidence that the current peaks come from FcMeOH molecules adsorbed onto the graphene surface. Figure 5c presents the anodic peak current (i_p) vs. scan rate (v), after appropriate background subtractions. The i_p-v curves are linear, as expected for the redox reaction of an adsorbed species (Section 1.5.4).

The surface concentration of adsorbed FcMeOH can be estimated based on the area underneath the cyclic voltammetry peaks according to Equation 1.13 in section 1.5.4. From a linear fit of the peak areas to the scan rate [Figure 2.11 (c)], we find a molecule coverage of $\Gamma = 1.1 \times 10^{-11}$ mol/cm^2. Assuming a ~4.5 Å diameter for FcMeOH molecules (*92*), this corresponds to ~1% of a monolayer coverage on the graphene surface. We also observed comparable adsorption coverage on bulk graphite surfaces (~2% monolayer coverage; see Appendix, Section 2.7.3). These values are considerably lower than the reported adsorption of ferrocene on glassy carbon electrodes modified by multi-walled carbon nanotubes (1.7×10^{-9} mol/cm^2) (*93*). We did not detect adsorption of FcMeOH on exfoliated graphene electrodes (Appendix, Section 2.7.3). Because of the much smaller area of these electrodes, we estimate that this measurement is not sufficiently sensitive when the surface coverage is below ~10%. The small FcMeOH coverage on CVD graphene suggests that the irreversible adsorption of FcMeOH occurs primarily at local defect sites.

2.5 Conclusion

In conclusion, we have performed electrochemical studies of individual monolayer graphene sheets derived from both mechanically exfoliated graphene and CVD graphene. Careful device design ensured that all redox reactions occur on clean graphene surfaces within well-defined areas. We found the electron transfer rates of graphene electrodes are more than 10-fold faster than the basal plane of bulk graphite, likely due to the presence of corrugations in the graphene sheets. We also demonstrated the electrochemical detection of adsorption and desorption of FcMeOH on CVD graphene. Our results demonstrate that electrochemistry provides a powerful means to investigate the interactions between molecules and the surfaces of graphene sheets used as electrodes.

2.6 Follow-up Studies on the Electron Transfer Kinetics of Graphene

The electron transfer kinetics on graphene have been further studied by different labs after our experiment. In particular, Tan *et al.* (*94*) in Prof. Abruña's group further studied the electron transfer kinetics on CVD graphene using scanning electrochemical microscope (SECM). Using ferricyanide [$K_3Fe(CN)_6$, an inner-sphere molecule that's more sensitive to specific chemical sites on the carbon surface and generally has slower kinetics (*72, 95*)] as mediator, they found the electron transfer kinetics is faster at defects/edges than at the basal plane of CVD graphene. Ritzert *et al.* (also in Prof. Abruña's group) systematically studied the standard transfer rate (k^0)

of more types of redox molecules on CVD graphene using SECM (*96*). The obtained k^0 values were also generally greater than those reported for basal plane of graphite (*85*), with the k^0 value for FcMeOH being 0.02 cm/s, which is on the same order of magnitude as our cyclic voltammetry results. These studies provide more insights on the electron transfer kinetics on CVD graphene surface.

Valota *et al.* (*97*) at University of Manchester (United Kingdom) studied the electron transfer kinetics of ferricyanide on individual pieces of mechanically-exfoliated mono- to multi-layer graphene using similar device design and cyclic voltammetry measurement strategy. They found that k^0 of ferricyanide measured on single/bilayer graphene electrodes was two times *greater* than measured on *defect-containing* multilayer graphene electrodes, indicative of different origins of the fast kinetics on exfoliated graphene other than defects or edges, likely related to the presence of corrugations in the graphene sheets as we originally proposed while keeping in mind the even larger k^0 values on single wall carbon nanotubes.

In addition, similar graphene working electrode structure and measurement strategies have been later adapted to characterize the self-assembly of molecules that were synthesized to specifically attach to graphene surfaces through non-covalent interactions (*98*).

2.7 Appendices

2.7.1 Resistance Correction for Cyclic Voltammograms of the CVD Graphene Electrode

Table 2.1 summarizes the voltammetric data for the cyclic voltammograms presented in Figure 2.8 before and after correcting the contact resistance between graphene and the electrode (~1100 Ω).

Table 2.1: The voltammetric data for the cyclic voltammograms presented in Figure 2.8 before and after resistance correction.

v (V/s)	i_{pc} (μA)	i_{pc}^{corr} (μA)	i_{pa} (μA)	i_{pa}^{corr} (μA)	ΔE_p (mV)	ΔE_p^{corr} (mV)
0.200	0.585	0.586	0.624	0.624	69.8	68.6
0.250	0.650	0.650	0.689	0.689	70.6	69.4
0.300	0.708	0.708	0.750	0.750	71.4	69.8
0.350	0.761	0.761	0.804	0.805	72.4	70.8
0.400	0.809	0.809	0.855	0.856	73.0	71.4
0.450	0.855	0.856	0.905	0.905	73.8	72.0
0.500	0.899	0.899	0.951	0.951	74.4	72.6

i_{pc}, i_{pa}, and ΔE_p: the catholic, anodic peak current, and the peak separation before resistance correction. i_{pc}^{corr}, i_{pa}^{corr}, and ΔE_p^{corr} :the catholic, anodic peak current, and the peak separation after resistance correction.

The discussions in the main text (Figure 2.8 and Figure 2.9) are based on the voltammetric data after resistance correction. To make sure that the relatively high k^0 value we obtained on the CVD graphene electrode is not an artifact resulting from overcorrection of resistance, here we also present a calculation of the effective area and k^0 without resistance correction.

Figure 2.12 (a) shows a linear fit of the uncorrected anodic peak current (i_{pa}) versus the square root of the potential san rate ($v^{1/2}$). Good linearity is still found

between i_{pa} and $v^{1/2}$. The effective area of the graphene electrode determined from the fit is 0.172 mm^2, which is the same as obtained after resistance correction (Figure 2.8).

Figure 2.12 (b) shows the uncorrected peak separation and the corresponding Nicholson's kinetic parameter ψ. Following the same procedure as described in the main text, a k^0 value of 0.037 cm/s is determined. This value is ~90 % of the k^0 (0.042 cm/s) presented in the main text, indicating the resistance correction only has a minor effect on the final k^0 result. Hence we conclude that the relatively high k^0 value on the CVD graphene electrode is not an artifact from resistance overcorrection.

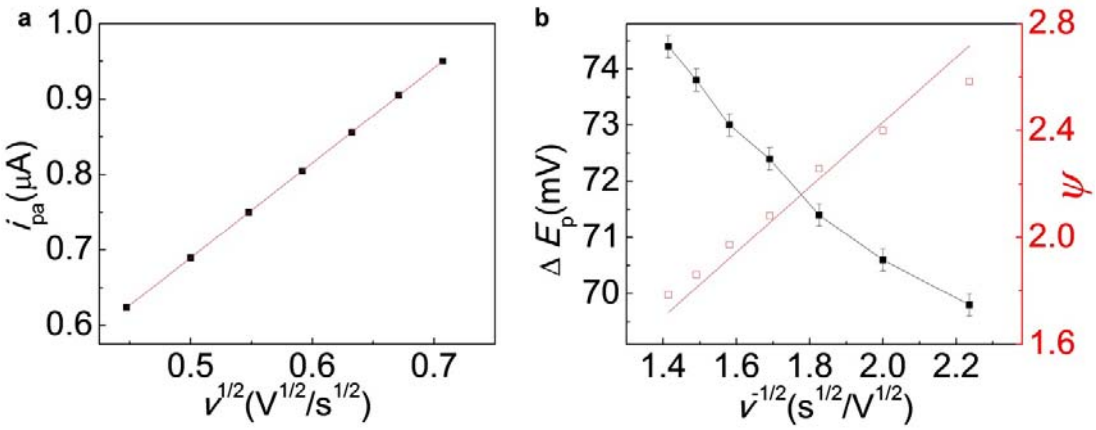

Figure 2.12: Analysis of the voltammetric data on CVD graphene electrode before resistance correction.

2.7.2 Electron Transfer Kinetics on the Basal Plane of Highly Ordered Pyrolytic Graphite (HOPG)

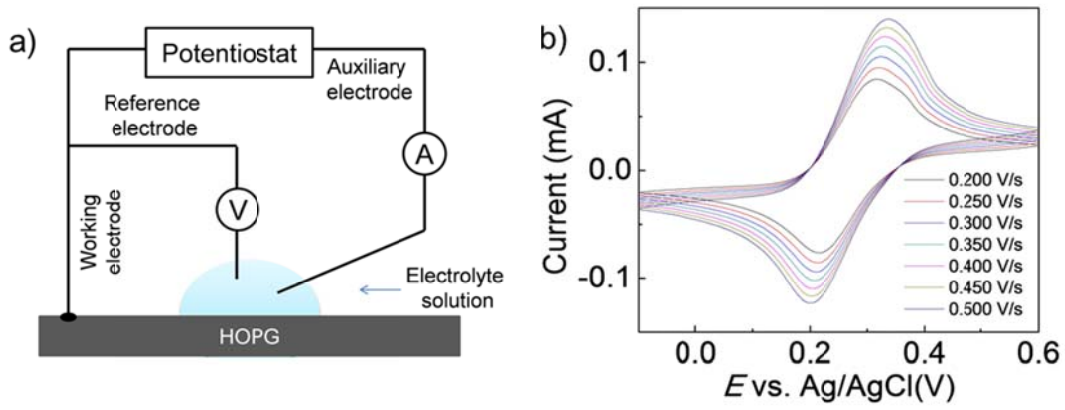

Figure 2.13: Electrochemistry on the basal plane of highly ordered pyrolytic graphite (HOPG).

(a) Schematic diagram of the inverted drop cell used to study the electrochemistry on the basal plane of HOPG. (b) Cyclic voltammograms of 1 mM FcMeOH in H_2O/0.1 M KCl measured on the HOPG basal plane at different potential scan rates (v).

k^0 on the basal plane of highly ordered pyrolytic graphite (HOPG) was measured with an inverted drop cell configuration [Figure 2.13(a)]. The HOPG basal plane was prepared by exfoliation and connected to the circuit with copper tape. A drop of electrolyte solution was then placed on top of the basal plane surface. An Ag/AgCl (saturated KCl) reference electrode and a Pt auxiliary electrode were lowered into the drop to complete the cell. This cell configuration eliminates possible impurities and damage to carbon surfaces (*99*).

Figure 2.13(b) shows the cyclic voltammograms of FcMeOH (1 mM) in H_2O/0.1 M KCl measured on the HOPG basal plane at different potential scan rates. Larger peak separations are observed in comparison to CVD graphene electrodes,

indicating slower electron transfer kinetics on the HOPG basal plane. Following the same analysis procedure as for the CVD graphene electrode, k^0 on the HOPG basal plane is determined to be 0.007 cm/s.

2.7.3 FcMeOH Adsorption on HOPG Basal Plane and Exfoliated Graphene Electrodes

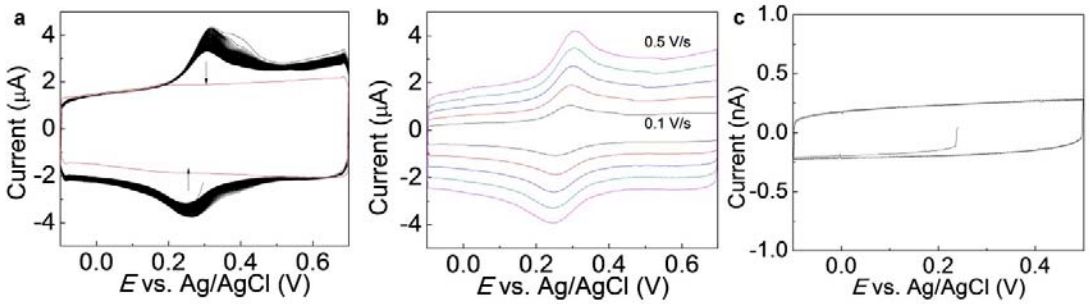

Figure 2.14: FcMeOH adsorption behavior on HOPG basal plane and exfoliated graphene electrode.

(a) Black line: repetitive cyclic voltammograms measured on the HOPG basal plane in H_2O/0.1M KCl solution, after adsorption of FcMeOH on the HOPG surface. Scan rate: 0.4V/s. Gradual desorption is observed over time. Red line: background voltammogram of the same HOPG basal plane before FcMeOH adsorption. (b) Cyclic voltammograms measured at different scan rates after desorption has reached equilibrium. Curves from black to pink represent cyclic voltammograms measured at 0.1, 0.2, 0.3, 0.4, and 0.5 V/s, respectively. (c) Cyclic voltammogram measured in H_2O/1 M KCl solution with an exfoliated graphene electrode, after electrochemical measurement in 4.9 mM FcMeOH solution for 1.5 hours.

FcMeOH adsorption is also detected on the HOPG basal plane by voltammetric measurements. After voltammetric measurements with 1 mM FcMeOH solution for 15 min, the HOPG basal plane surface was rinsed with copious deionized

water and then assembled into the cell with a drop of H_2O/0.1M KCl solution with no FcMeOH added.

Figure 2.14 (a) shows the cyclic voltammogram thus measured on the HOPG basal plane surface, in which both oxidation and reduction peaks are observed. The peak current reduces during continuous voltammetric measurement and stabilizes at a finite value, indicating a portion of the adsorbed FcMeOH molecules gradually desorb from the HOPG surface, similar to what we observed on the CVD graphene electrode.

Figure 2.14 (b) shows the cyclic voltammograms measured at different scan rates after the voltammogram has stabilized. Using similar methods as for the CVD graphene electrodes (Fig. 4), we determine the surface coverage of FcMeOH to be 2×10^{-11} mol/cm^2. This value corresponds to ~2% of monolayer coverage, slightly higher than what we found for CVD graphene electrodes (1%).

In contrast, no measurable adsorption of FcMeOH is observed on electrodes made of exfoliated graphene sheets. Figure 2.14 (c) shows the cyclic voltammogram measured with one of our mechanically exfoliated graphene electrodes in 1 M KCl solution, after electrochemical measurement in 4.9 mM FcMeOH solution for 1.5 hours. No peaks corresponding to adsorbed FcMeOH molecules are found.

CHAPTER 3

LOW RESISTANCE MAGNETIC TUNNEL JUNCTIONS WITH GRAPHENE AS A TUNNEL BARRIER

3.1 Introduction

The field of spintronics benefits greatly from the tunneling magnetoresistance (TMR) effect. After more than 30 years of development (*57, 100-104*), the highest achieved room-temperature magnetoresistance is 604% (optimistic definition) in CoFeB/MgO/CoFeB magnetic tunnel junctions (MTJs) (*58*). This value goes up to 1144% at 5 K (*58*). The high room-temperature magnetoresistance makes MgO MTJs great for practical applications, including spin-transfer-torque magnetic random-access memory (STT-MRAM) and hard drive disk read heads (*59-61*). The extremely large magnetoresistance of MgO TMJs is considered to be caused by the spin filtering effect of the crystalline MgO barrier. In fact, theoretical calculations (*105, 106*) predicted a magnetoresistance in excess of 1000% for lattice-matched Fe/MgO/Fe TMJs before the first experimental results were published. The discovery of large magnetoresistance in MgO MTJs exemplifies a beautiful case in which theory provides valuable guidance for experiments.

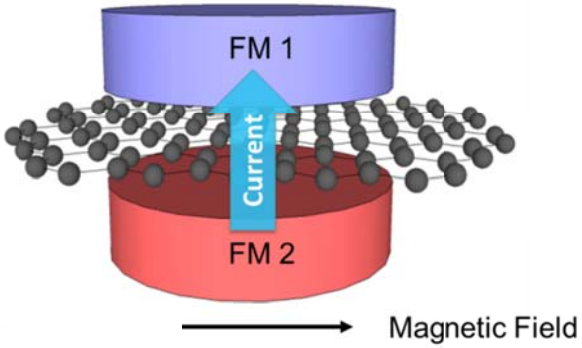

Figure 3.1: Conceptual diagram of the FM/ Graphene/FM junction.

Recent theoretical studies have predicted that graphene and graphite can be excellent spin filters in MTJs (*107-112*). In particular, lattice-matched FM/Gr_n/FM junctions (Figure 3.1), with FM being ferromagnetic materials and Gr_n being graphite with *n* layers of graphene, are expected to have magnetoresistances comparable to those of MgO MTJs, while at the same time achieving much lower junction resistances. In reality, under current technical limitations it may still take a great deal of efforts to realize FM/Gr_n/FM junctions with the desired lattice match. On the other hand, even without precise lattice matching, graphene, being a single layer of covalently-bonded carbon atoms, can potentially function as a unique barrier material that is ultrathin, pinhole-free, and highly ordered at the atomic scale. The exchange coupling between the two magnetic electrodes through graphene layer is also of scientific interest (*109*).

Recent studies have shown that graphene is a good spin-conserving medium with intrinsically weak hyperfine interaction and spin-orbit coupling. The spin-relaxation length in various types of graphene is found to be at the micron scale in the lateral direction at room temperature (*21, 113-115*). A 10% magnetoresistance was

measured in a two-terminal lateral graphene spin valve device (*116*). In the meantime, experimental studies on vertical electron/spin transport through graphene have just started (*117, 118*).

This chapter presents our efforts to experimentally study FM/Gr_n/FM junctions. In particular, we have developed a novel fabrication process (Section 3.3) that aims to achieve intrinsic FM/graphene interfaces without oxidation of the ferromagnetic materials. Electrical characterizations (Section 3.4 and 3.5) indicate that the junctions are tunnel junctions with 1-4% magnetoresistance and low *RA* product ranging from 3 to 10 $\Omega\mu m^2$.

3.2 Previous Studies on Graphene-based Magnetic Junctions

3.2.1 Theoretical Prediction: Graphene and Graphite as Excellent Spin Filters

Theoretical studies on graphene-based magnetic junctions were pioneered by Karpan *et al.,* who predicted that graphene can function as an excellent spin filter in FM/Gr_n/FM junctions (Figure 3.1). Using a pessimistic definition (Equation 1.14; Here we use R_P and R_{AP} to denote the junction resistance under parallel and antiparallel alignments of the electrode magnetization, respectively), the spin-filtering effect of a single graphene layer was found to be strong enough to generate a 20% magnetoresistance (MR). Stronger MR was calculated as the number of graphene layers increases, and the MR for a junction with 3-layer graphene can be as high as 90% (Figure 3.2). If we convert the values to the more frequently used optimistic form

(Equation 1.15), the MR will be 25% for junctions made of single-layer graphene, and almost 900% for junctions containing more than 3 layers of graphene, comparable to the highest MR achieved in MgO junctions at low temperature. (*58*)

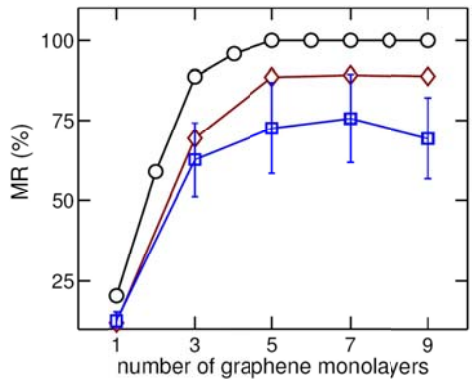

Figure 3.2: The calculated magnetoresistance of a Ni/Gr_n/Ni junction as a function of number of graphene monolayers.
Black Circles: Ideal junctions; Diamonds: Ni/Gr_n/$Cu_{50}Ni_{50}$/Ni junctions where the interface layer is a disordered alloy; Squares: Ni/Gr_n/ Ni junctions where the top layer of one of the electrode is rough with only half the sites occupied. (*107, 108*)

The abovementioned strong spin-filtering effects require an epitaxial lattice match between graphene and the (111) planes of the ferromagnetic materials. Experimentally, although this epitaxial lattice match may be non-trivial to realize, graphene and ferromagnetic materials such as Co and Ni have very close lattice constants (Table 3.1). The AC and BC configurations between graphene and the TM (111) plane are found to be theoretically stable, with layer distances of 0.2 and 0.3 nm, respectively (Figure 3.3) *(107, 108).* Lattice mismatch, disorder and roughness at the interfaces reduce the spin-filtering effect, as will be discussed below.

Table 3.1: Lattice constants of graphene, cobalt, nickel, and copper

	Graphene	Cobalt	Nickel	Copper
Lattice constants [exp] (nm)	0.246	0.2506	0.2492	0.2556

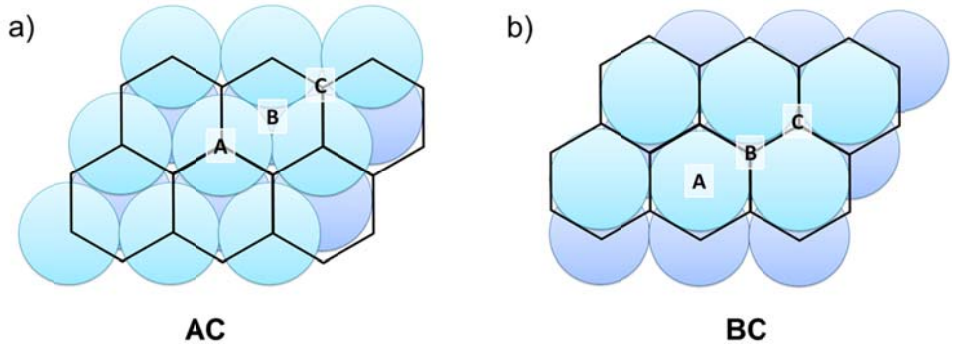

Figure 3.3: The AC and BC lattice configuration of graphene on FM (111) plane

Black Hexagons: Graphene lattices; light blue balls: the top layer of FM atoms (A lattice); dark blue balls: the second layer of FM atoms (B lattice). The third layer of atoms (C lattice) is not plotted in the figure.

In a simplified model, the spin-filtering effect of graphene can be interpreted by comparing the Fermi-surface of graphene with the projected Fermi-surface of ferromagnetic materials onto the (111) plane (Figure 3.4). As shown in Figure 3.4 (f), the Fermi-surface of graphene/graphite is centered at and very close to the highly symmetric K/K' points. In contrast, Co and Ni don't have majority spin states close to the K/K' points, but have the minority spin states spanning all over the first Brillouin zone [Figure 3.4 (a-d)]. As a result, only the minority spin states close to the K/K' points should contribute to the transmission from a close-packed (111) ferromagnetic material surface into graphene/graphite. Charge carriers in other regions of one of the

electrodes, including all the majority spin-states, would have to tunnel through graphene/graphite to reach the other electrode. If the graphite is thick enough to suppress tunneling, the majority-spin conductance will be quenched and only the minority-spin conductance through the graphite will survive (Figure 3.5). Excellent spin filtering will occur when the magnetizations of the two ferromagnetic electrodes are parallelly aligned, while for antiparallel alignments the conductance will vanish. The above argument predicts strong spin filtering effects when lattice matching between graphene and the (111) plane of the ferromagnetic materials is achieved so that the first Brillouin zones of the graphene and the ferromagnetic materials are relatively aligned in the way shown in Figure 3.4.

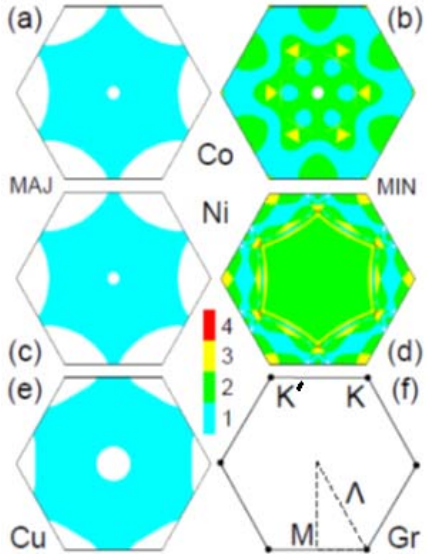

Figure 3.4: The Fermi-surface projections onto (111) for ferromagnetic materials and the Fermi-surface of graphene in 2D 1st Brillouin zone.

(a) and (b): The Fermi-surface projection for minority (a) and majority (b) spins of Co; (c) and (d): The Fermi-surface projection for minority (c) and majority (d) spins of Ni;

e): The Fermi-surface projection for copper. (f) The Fermi-surface of graphene in the 1st Brillouin zone, which centers at the highly symmetric K/K' points. (*107, 108*)

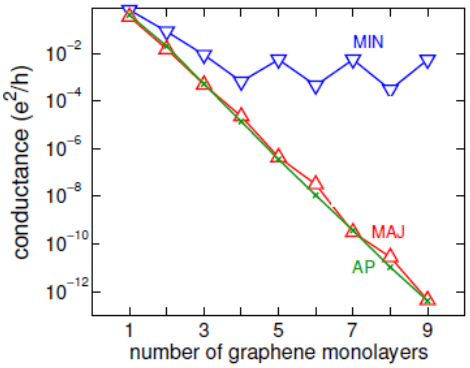

Figure 3.5: The calculated conductance of different spin channels in a Ni/Gr$_n$/Ni junction as a function of the number of graphene layers.
Blue triangles: conductance of the minority spin channel in parallel magnetization; Red triangles: conductance of the majority spin channel in parallel magnetization; Green crosses: conductance in antiferromagnetic alignment. The conductance is normalized to the 1×1 surface unit cell used for the ideal case. (*107, 108*)

Karpan *et al.* also systematically studied the robustness of the spin filtering effect in various non-ideal conditions (*107, 108*). They found roughness and disorder of one of the two FM/graphene interfaces reduce the expected MR by 30% and 10%, respectively (Figure 3.2, squares and diamonds). In addition, the spin-filtering effect may reduce when the distance between metal and graphene is too small so that the interaction between the carbon and ferromagnetic atoms needs to be considered. Such interaction may open a gap in the graphene band structure, in which case there will be no states for graphene at the K/K' points for minority spin carriers to transmit, and so the spin-filtering effect is quenched.

More recently, Saha *et al.* (*111*) studied the bias dependence of AC- and AB-stacked Ni/Gr_5/Ni junctions using a Green's function formula combined with density functional theory. They found close to 100% pessimistically defined MR at zero bias for FM/Gr_n/FM junctions with n = 5, in agreement with the results from Karpan *et al.* (*107, 108*). In addition, they found the MR persists up to a bias voltage of 0.4 V. On the other hand, Li *et al.* (*119*) found a spin-flip mechanism at Co/Graphene interfaces due to the antiferromagnetic coupling between the graphene and Co layers via *pd*-π interactions. This mechanism may reduce the spin injection efficiency at the Co/Graphene interfaces and thus reduce the magnetoresistance of the junction.

3.2.2 Previous Experimental Studies and Possible Oxidation Issues in the Fabrication Process

Experimental studies on FM/Graphene/FM junctions were first carried out by Cobas *et al* (*117*). A 2% magnetoresistance was reported for micro-fabricated Py/Graphene/Co junctions (Py being Permalloy; Figure 3.6) at 4 K, which persisted up to 400 K (Figure 3.7). The relatively small magnetoresistance in comparison to the theoretical prediction was considered to be caused by the roughness and disorder at both FM/graphene interfaces. However, it should be noted that the reported resistance-area (*RA*) products of the junctions in the study were excessively large (35,000-75,000 $\Omega.\mu m^2$). As a comparison, the *RA* product for a junction with 1.5 nm-thick single crystal MgO is 50-100 $\Omega.\mu m^2$ (*102*). Graphene is generally considered as a zero-gap semiconductor (*2*), and its thickness is ~0.4 nm (*3*). The *RA* product of FM/Graphene/FM junction thus should not be greater than the value for 1.5 nm-thick MgO junctions.

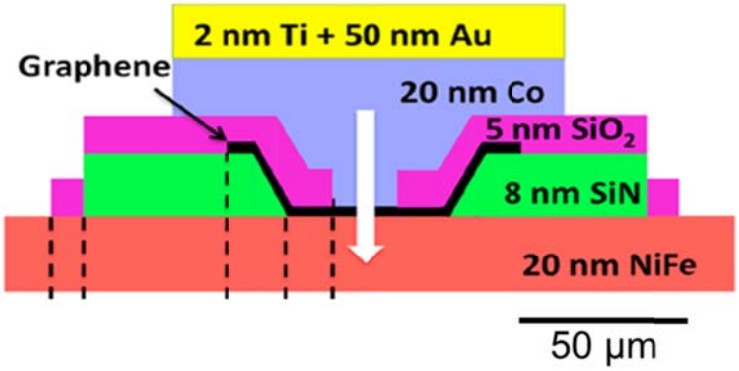

Figure 3.6: The devices structure for Co/Graphene/Py junctions in ref (*117*)

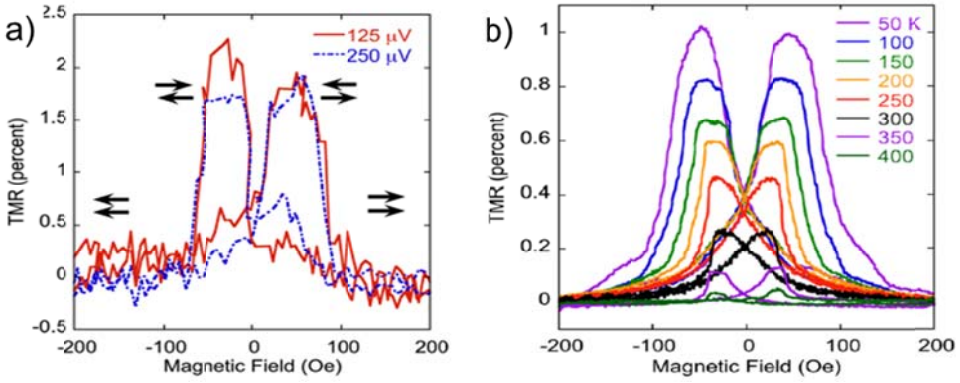

Figure 3.7: The magnetoresistance of Py/Graphene/Co junctions reported in ref (*117*)

We suspect that the unexpectedly large *RA* values reported by Cobas *et al.* (*117*) are likely caused by the oxidation of the ferromagnetic materials at the FM/graphene interfaces during the fabrication process. CVD graphene grown on copper foils was used in the junctions. In order to transfer the graphene onto the device substrate, Poly(methyl methacrylate) (PMMA) film supported graphene was first floated on the surface of a water bath after removal of the copper foil. The target substrate containing the pre-deposited permalloy electrodes was then inserted into the

water to scoop up the graphene (Figure 3.8). The graphene then made contact with the permalloy electrode after the water between the graphene and the permalloy electrodes was dried in air or by blowing with N_2. Exposure of the permalloy electrode to air and water during this process may cause oxidation of the permalloy, and consequently lead to very large *RA* values.

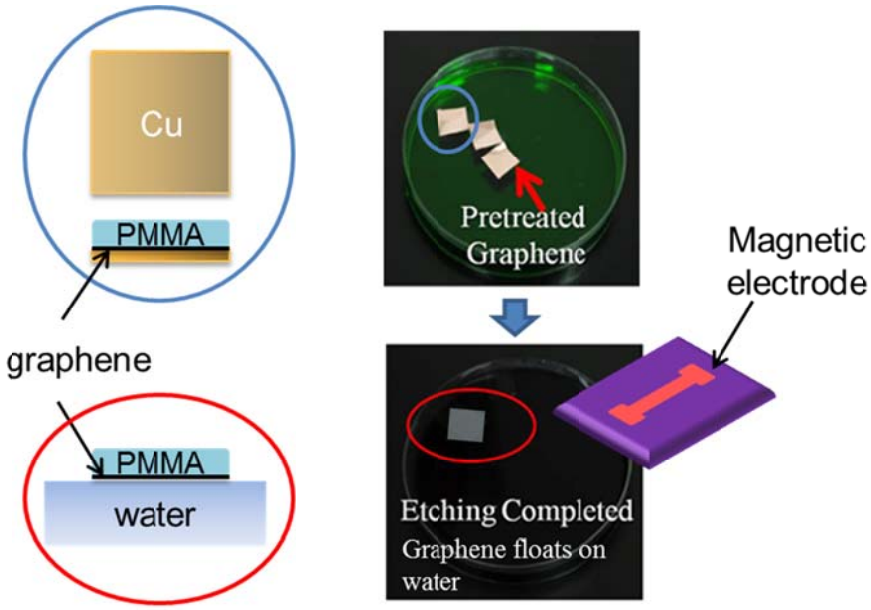

Figure 3.8: The graphene transfer process used in previous studies may cause oxidation of the ferromagnetic electrode.

3.3 Fabrication Strategies to Avoid the Oxidation Issue

To avoid the abovementioned oxidation issue, we must avoid transferring graphene onto the surface of a pre-deposited magnetic electrode. One possible approach is to first prepare a suspended graphene sheet, and then deposit FM materials onto the graphene surface. The FM materials at the FM/graphene interfaces are then

automatically protected by graphene, and thus should have minimum-to-no oxidation. Graphene, despite of being a single layer of carbon atoms, is found to be a good barrier against oxidation (*120*). Thus it's unlikely that the interfacial ferromagnetic material will be oxidized through graphene even when the device is exposed to air. However, because suspended graphene is very fragile, we found that it's not feasible to deposit thick magnetic materials onto a free-standing suspended graphene. We thus developed a two-step-evaporation process that takes advantage of the PMMA protection layer used in the graphene transfer process. In this section we will discuss the device structure and fabrication processes we designed to make suspended, non-oxidized FM/graphene/FM junctions with high yield.

3.3.1 Device Structure

Figure 3.9 illustrates the structure of our device (not to scale). The junction is located at the region in the red box where a piece of suspended graphene is sandwiched between the two ferromagnetic electrodes. The lateral size of the junction is defined by the diameter of the hole in the Si_3N_4, and it ranges from 250 nm to 3.2 μm in diameter. Along the vertical direction, the top electrode consists of 60 nm Co/120 nm Au, and the bottom electrode consists of 60 nm permalloy (Py, $Ni_{80}Fe_{20}$) / 600 nm Cu/ 60 nm Au. Here, Py and Co are chosen for their different coercive fields.

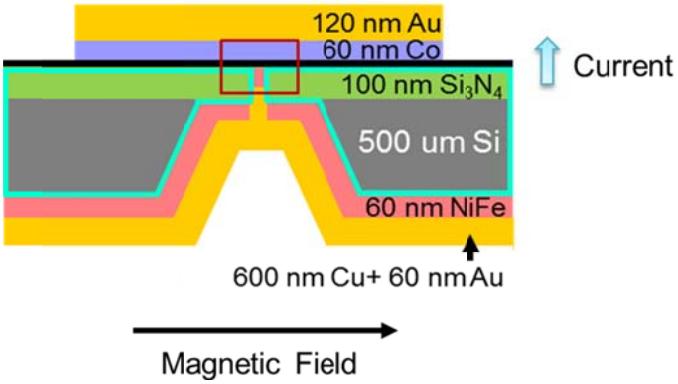

Figure 3.9: The structure of our device

Not to scale. The red box highlights the Py/Graphene/Co junction.

3.3.2 Fabrication Process

The graphene we used in our devices was grown by chemical vapor deposition (CVD) on copper foils (*15*). When compared to exfoliated graphene, CVD graphene can be readily prepared in large sizes, e.g., a few centimeters by a few centimeters. This enabled us to batch produce large number of devices on the same substrate. In our experiment, substrates are prepared to have 64 devices placed in an 8×8 matrix, with each individual device having the size of 3×3 mm. The 64 devices are fabricated in parallel through all the fabrication steps, and are divided apart in the end for electrical characterizations.

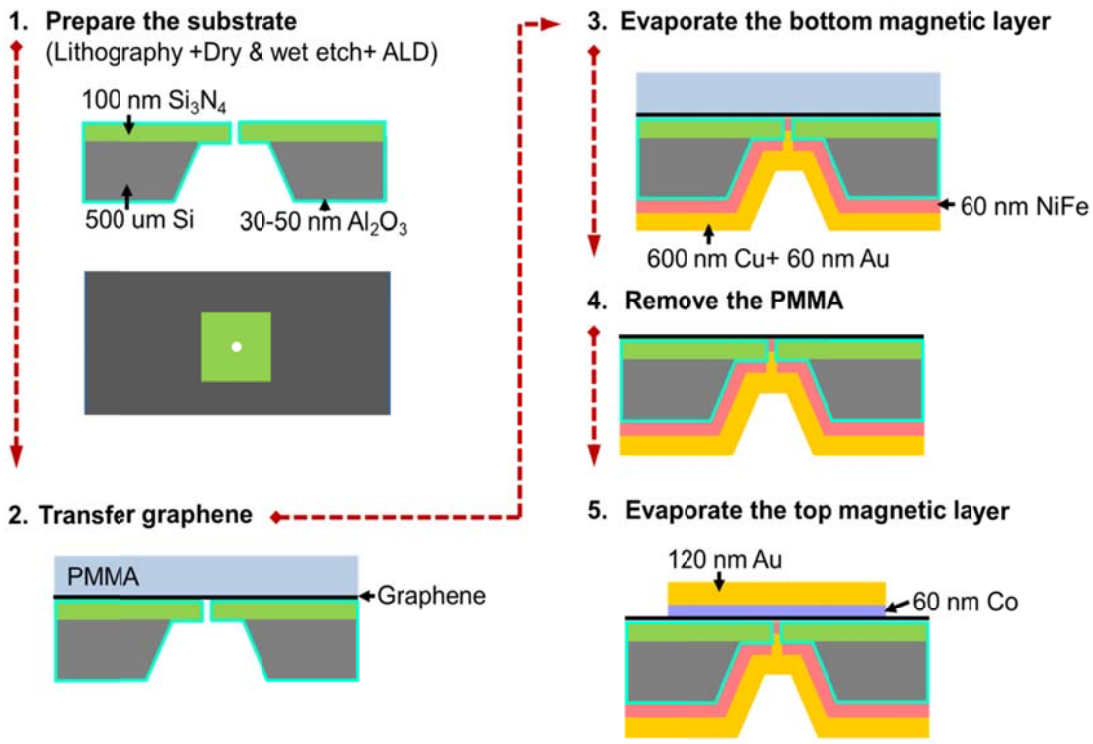

Figure 3.10: Major fabrication steps for our FM/graphene/FM junctions.

Figure 3.10 shows the major steps we used to fabricate the devices. Substrates were prepared in the first step. The fabrication process for this step was adapted from the methods our group previously developed for studies on metal quantum dots (*121, 122*). Sequential steps of e-beam lithography, plasma etching, photolithography, KOH etching, and atomic layer deposition (ALD) were employed (explained in more detail in the Appendices, Section 3.7.1). Starting from a 4-inch wafer, after the first step six substrates were obtained, each containing 64 devices aligned in an 8×8 matrix. The substrate structure for an individual device is illustrated in Figure 3.10 (step 1). A ~100 nm thick, 100 ×100 μm membrane of Si_3N_4 was suspended in the center of the device. A hole to suspend graphene in later steps was etched in the center of the

suspended Si_3N_4 membrane. The whole substrate is conformally coated with 30-50 nm of ALD-grown Al_2O_3 to further ensure electrical insolation between the top and bottom surfaces of the device. Figure 3.11 shows the SEM images of the holes on the Si_3N_4 membrane after step 1.

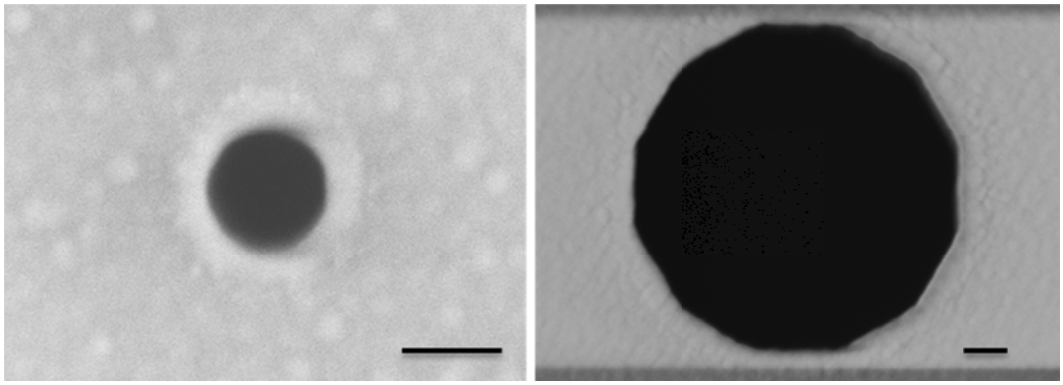

Figure 3.11: The SEM images of the holes on Si_3N_4 membrane after step 1.
Scale Bars: 200 nm

Graphene was next transferred onto the substrate following the standard PMMA recipe (Figure 3.10 step 2) (*15*). At the end of this step, graphene is suspended over the hole on the Si_3N_4 membrane. Notice that the PMMA layer was kept on top of graphene in this step: it was used as a supporting layer for the evaporation of the bottom electrode in the next step.

Next, the bottom electrode was evaporated onto the graphene surface. An evaporator capable of angle evaporation (Sharon) was employed. A 60 nm thick permalloy (NiFe) layer was first evaporated perpendicularly to the substrate using a thermal source. Without breaking vacuum, copper (600 nm) and gold (60 nm) were then e-beam evaporated at ± 36 degrees with respect to the perpendicular direction

(Figure 3.12). A relatively thick copper layer was used and evaporated at different angles to ensure that the Py at the junction connects to the metal at the bottom surface of the device, which was used to connect to external circuits for measurement. The gold layer serves as a capping layer to protect the underneath copper from oxidation.

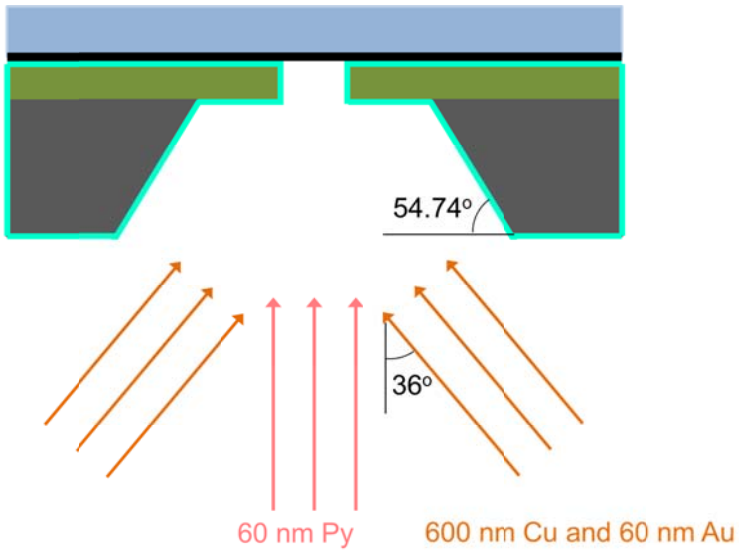

Figure 3.12: Scheme for the angle evaporation used to deposit the bottom electrode

After deposition of the bottom electrode, the PMMA layer was removed by placing the devices in a 1:1 acetone : dichloromethane solution overnight. The device was then rinsed with isopropyl alcohol and dried under blowing N_2.

Figure 3.13 shows a partially fabricated device after step 4. This optical image [Figure 3.13 (a)] was taken from the top of the device, and the junction corresponds to the central, bright yellow region. Here the bottom Py electrode is visible through a transparent graphene layer. The junction appears to suspend completely over the region. A Raman spectrum [Figure 3.13 (b)] at the center of the junction region [blue

circle in Figure 3.13 (b)] produced pronounced 2D and G peaks, with the 2D peak being more than two times higher than the G peak, thus confirming the existence of monolayer graphene over the junction region. In addition, no D peak is observed above the noise level, indicating a reasonably high quality of graphene.

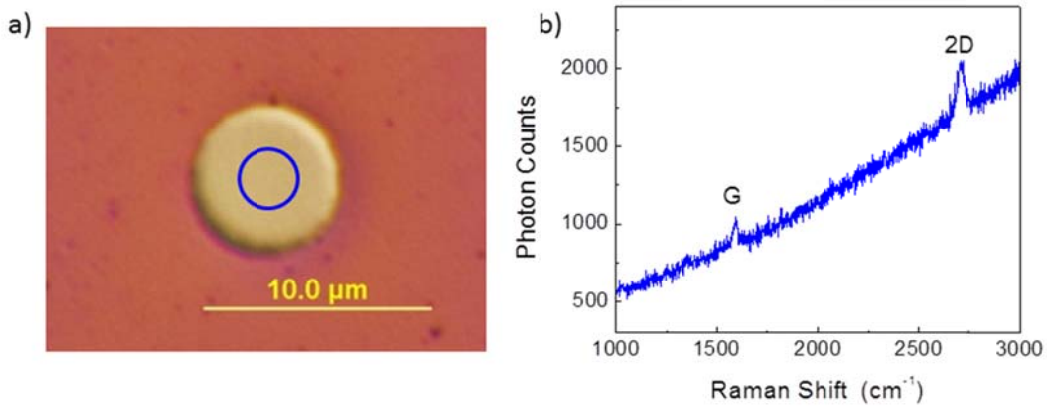

Figure 3.13: Optical image of the junction and Raman spectrum of graphene taken after step 4.
Blue circle in (a) indicates the region in which the Raman spectrum in (b) was taken.

The top magnetic electrode was then deposited on top of the graphene junction (Figure 3.10, Step 5). A 60 nm cobalt layer and a 120 nm gold layer were deposited perpendicularly to the substrate using e-beam evaporation. A shadow mask was used to ensure that the cobalt and gold were only evaporated onto the central 2×2 mm^2 region of the device. This avoids the potential contact between the top electrode to the bottom electrode through the edge of the devices rather than through the junction. The fabricated devices were divided apart for electrical measurement. SEM images of the junctions, after all the fabrication processes were complete, are given in Figure 3.15.

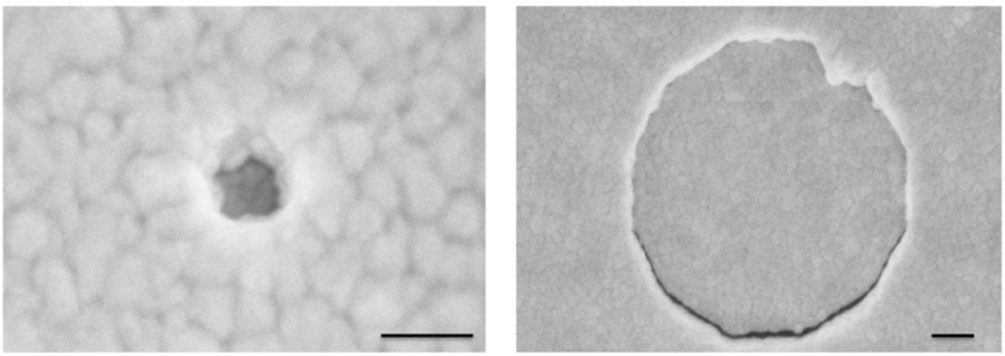

Figure 3.14: SEM images of the junctions after fabrication processes were complete.

Complete, smooth electrodes are suspended over the junction region, confirming success of the fabrication process. Scale bars: 200 nm

3.4 Measurement Setup

3.4.1 Device Mounting

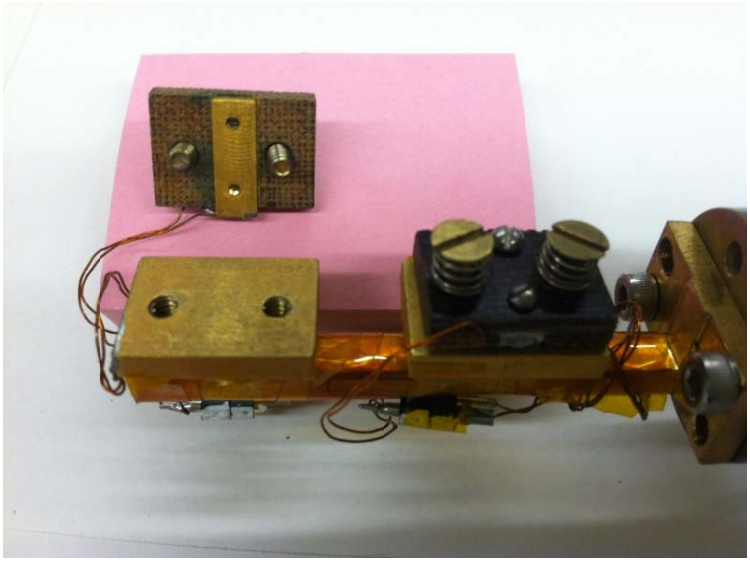

Figure 3.15: Photograph of the home-built device holder

Due to the special 3D geometry of our device that the two electrodes are located respectively on the top and bottom surfaces, common contacting methods such as micro probes or wire bonding are not suitable for our electrical measurements. The device was, instead, mounted in a home-built sample holder designed to make electrical contacts to devices from bottom and top surfaces (*121, 122*). Figure 3.15 shows a photograph of the sample holder. Two metal plates (made of gold plated copper) contacted the device in a sandwich geometry. The two plates were electrically isolated from each other except for through the device. Screws with springs were loaded from the top to press down on the top plate and ensure reliable electrical contacts.

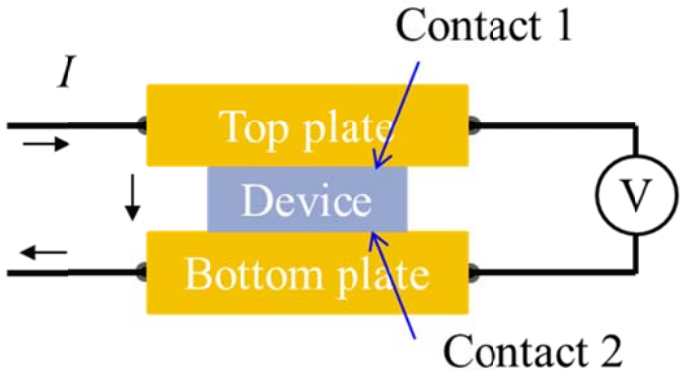

Figure 3.16: The pseudo-four-point measurement scheme used in measurement

$$R_{measurement} = R_{junction} + R_{contacts} + R_{electrode} \qquad \text{Equation 3.1}$$

The two metal plates were connected to the measurement circuits in a pseudo-four-point configuration. (Figure 3.16) This configuration is efficient in removing the

resistance of the wires/contacts between the plates and the measurement equipment. However, it's "pseudo-four-point" as the measured resistance still includes the contact resistance between the plates and the electrodes, as well as the resistance of the electrodes themselves (Equation 3.1). Thus when mounting the device, it's important to make sure the device contacts well with the top and bottom metal plates. For example, equal pressure should be applied from the two springs to prevent sample tilting. In addition, the pressure should be just right to provide large enough pressure to clamp the sample in place, but not too large to make the contact between the metal plates and device too rigid: we observed increases in measured resistance when the screws were too tight, indicating increases of contact resistances between the plates and the electrodes. Meanwhile, the resistance of the electrodes of the device is estimated to be less than 0.2-0.3 Ω from our device geometry, mostly contributed from the bottom permalloy electrode (modeled as a 250 nm diameter and 60 nm thick nano-pillar). This value is much smaller than the resistance of the device (a few tens of Ωs), and thus can be ignored in our magnetoresistance transport studies.

3.4.2 Low Temperature Measurement

Low temperature measurements were carried out with a 3He-MMS cryostat (Desert Cryogenics, LLC), which was operated in the temperature range from 4 K to 200 K in our experiment. The base temperature of 4 K was provided by the liquid helium environment in a standard helium dewar, while measurement at higher temperatures was carried out either during the quasi-static system cool down process or with a heating resistor that brings up the system temperature after base temperature

was reached. The temperature of the sample holder was read out and controlled by a Lakeshore 200 temperature monitor. Magnetic field was applied to the device in the in-plane direction with a superconducting niobium-tin coil that was integrated to the cryostat. The coil was carefully calibrated with a Hall sensor at low temperature to ensure accurate read out of the field strength.

3.5 Results and Discussions

3.5.1 Low Resistance-Area Product of Our Py/Graphene/Co Junctions

Table 3.2: Resistance-area products of representative junctions measured in our study

Device Name	Diameter (μm)	Resistances (Ω)	*RA* product (Ω.μm^2)	*MR_Low T* (%)	*MR_Room T* (%)
W4-IV-B1	0.25	55.8	2.7	1.8	0.7
W4-IV-F5	0.25	71.2	3.5	2.5	1.7
W4-IV-D4	0.25	64.5	3.2	3.4	0.9
W4-IV-C2	0.25	440	21.6	1.5	0.9
W4-IV-A2	0.25	30.6	1.5	N/A	0.9
W4-IV-D2	0.25	126	6.2	N/A	1.3
W3-B-D6	0.34	37	3.4	N/A	0.3
W3-B-C6	0.74	10.8	4.6	N/A	0.7
W3-B-F4	1.36	54.5	79.1	N/A	0.5
W3-B-B6	1.74	28.8	68.4	0.8	0.3

Table 3.2 presents the diameter, resistance, and corresponding *RA* products of ten representative junctions measured in our study. A *RA* product of 3-10 Ω.μm^2 is found for most junctions. This value is about 10^4 times lower than the value previously

obtained by Cobas *et al.* (35,000-75,000 $\Omega.\mu m^2$) (*117*). As discussed previously (Section 3.2.2), the *RA* product for FM/graphene/FM is not expected to be greater than the value reported for junctions with 1.5 nm-thick MgO as the tunnel barrier (50-100 $\Omega.\mu m^2$) (*102*). The exceedingly large *RA* product reported in the previous study (*117*) is likely caused by the oxidization of the magnetic material at the FM/graphene interface during fabrication (Section 3.2.2). In contrast, the low *RA* product obtained in our study suggests a more successful avoidance of the surface oxidation issue with our fabrication strategy (Section 3.3).

We note that the experimental *RA* products of three devices fall into the range of 20-80 $\Omega.\mu m^2$. Although still quite small in value, they are significantly larger than the values obtained from the other seven junctions. The greater *RA* products seem to correlate with a larger junction size. As mentioned in section 3.4.1, the pseudo-four-point configuration we used to measure the junction resistance includes the contact resistance between the sample holder (metal plates) and the device electrodes. Such resistance is expected to influence the *RA* products more significantly for larger junctions simply because they have smaller intrinsic resistance. Another possible source of large *RA* products could be residual of PMMA films on graphene, which could occasionally block a portion of the junction area and reduce the effective junction area.

The existence of graphene domain boundaries could also potentially account for the apparently larger *RA* products of the large junctions. Since the CVD graphene we grew has typical domain size of 500 nm-1 μm (Chapter 1), junctions larger than ~1

μm in diameter should contain a few graphene domains in the junction area, whereas smaller junctions are more likely to contain single-domain graphene. The influence of graphene domain boundaries on transport properties has been a very interesting research topic. Theoretical study predicted that certain types of domain boundaries will open a band gap that is as large as 1 eV in graphene (*123*). This prediction is supported by a recent experimental study at Cornell, which found that domain boundaries contribute extra resistance in lateral (in-plane) transport, presumably through charge carrier scattering (*124*). There is, however, no experimental study on how graphene domain boundaries may influence vertical transport to date. The possibility that domain boundaries in large junctions may lead to higher resistance is highly intriguing, and may be further studied with our current junction structure. The domain structure of suspended graphene on Si_3N_4 membrane can be readily checked with dark-field TEM (*17, 18*) even in the presence of a supporting PMMA layer. Thus, in our future research, a dark-field TEM step could be added after Step 2 of our fabrication (Figure 3.10) to examine the domain structures at the junction. We would then be able to study the relationship between the domain structure of graphene and the vertical electrical/spin transport properties of each junction.

3.5.2 Bias and Temperature Dependences of the Junction Resistance

While achieving low *RA* products, bias and temperature dependences of the junction resistance indicate charge carriers transport through graphene through tunneling.

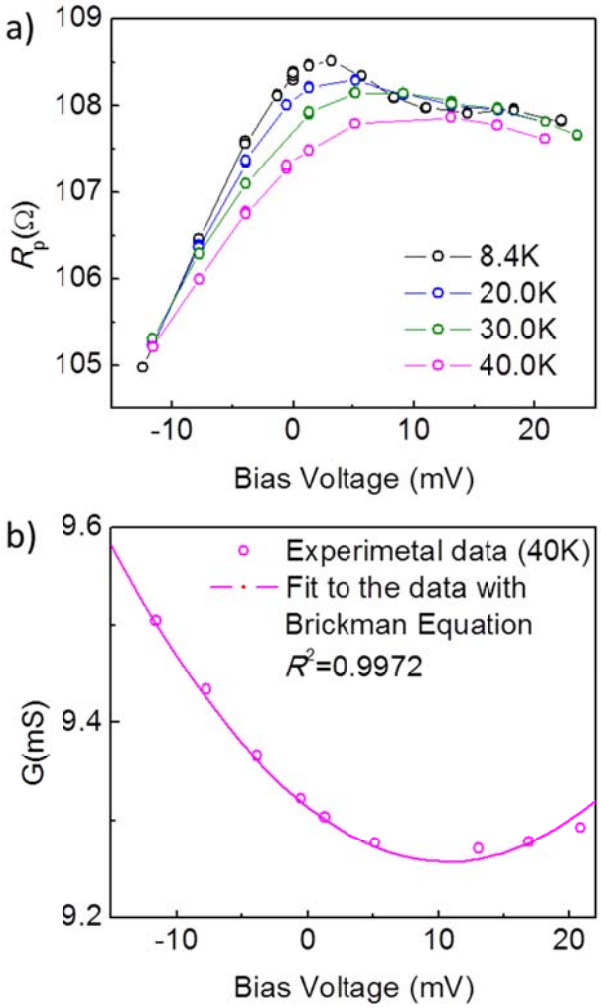

Figure 3.17: The bias dependences of the junction resistance.
(a) Differential resistance of a representative Py/Graphene/Co junction at different DC bias voltages at four different temperatures. The junction was polarized in a parallel alignment with a magnetic field of 1500 Oe. (b) Fit to the experimental data at 40.0 K with the Brickman model.

Figure 3.17(a) shows the measured differential resistance (R = dV/dI) of a representative Py/Graphene/Co junction at different DC bias voltages. The differential resistance peaks at a bias voltage that's close to zero and decreases with increasing bias, consistent with tunneling transport (*125*). The bias dependence of the differential

resistance exhibits a clear asymmetry, decreasing faster in the negative bias direction. Similar asymmetry was observed in all the characterized junctions with the same polarity (Appendices, Section 3.7.3). This asymmetry is likely caused by the different work functions of the two different ferromagnetic materials used in the junctions (*126*).

The barrier parameters can be roughly estimated by fitting the bias dependence data to the Brickman model (*126*), which for differential conductance gives:

$$\frac{\mathrm{d}I}{\mathrm{d}V} = 3.16\times10^{10}\,\frac{\sqrt{\bar{\varphi}}}{t_b}\,e^{-1.025 t_b\sqrt{\bar{\varphi}}}\left(1-0.0426\frac{t_b\Delta\varphi}{\bar{\varphi}^{3/2}}V+0.0327\frac{t_b^{\,2}}{\bar{\varphi}}V^2\right)A \qquad \text{Equation 3.2}$$

where $\bar{\varphi}$ (in eV) and t_b (in Å) are respectively the effective height and thickness of the tunnel barrier, and $\Delta\varphi = \varphi_{left} - \varphi_{right}$ (in eV) is the difference between the work functions of the two electrodes. A is the junction area, and is measured in cm^2. Figure 3.17 (b) shows our fitting result. The data at 40 K were used for this fitting as data collected at lower temperatures were complicated by a pronounced peak at bias voltages below 10 mV, attributable to the so-called zero-bias anomaly caused by spin-flip scattering during the tunneling process (*127, 128*). Our best fit was obtained for

$$\begin{aligned} t_b &= 12.1\pm0.1\ \text{Å} \\ \bar{\varphi} &= 90\pm3\ \text{meV} \\ \Delta\varphi &= 59\pm3\ \text{meV} \end{aligned}, \qquad \text{Equation 3.3}$$

roughly consistent with a thin tunnel barrier expected for FM/Graphene/FM junctions. Although graphene is a zero-gap semiconductor in its free-standing state, theoretical studies suggested that interactions between graphene and neighboring electrode atoms may open a gap in graphene (*107, 108*). This could explain the non-zero barrier height we obtained from fitting.

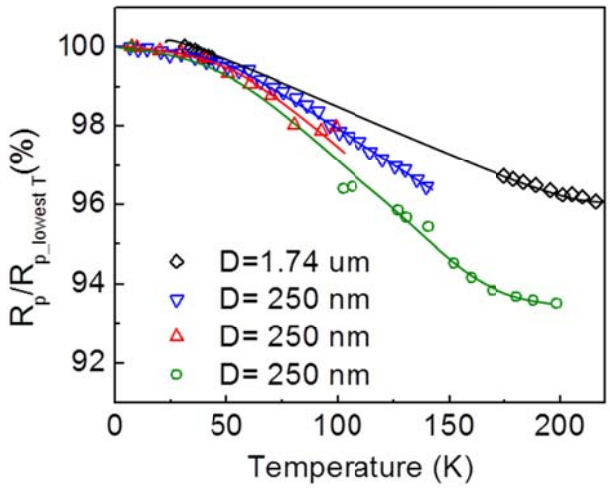

Figure 3.18: Temperature dependences of the junction resistance.
The junction was polarized in a parallel alignment with a magnetic field of 1500 Oe.

Figure 3.18 shows the temperature dependence of the resistance of four different junctions, defined as $R_p(T)/R_p(low\_temperature)$. The resistance of all four devices increases moderately as the temperature decreases, again consistent with tunneling transport through a weak barrier (*129*).

3.5.3 Magnetoresistance Response of the Junctions

The magnetoresistance response of the junctions was measured by recording the resistance of the junctions under a varying magnetic field. Figure 3.19 shows the

representative *resistance* vs. *field* curves measured with a large [>1 μm in diameter; (a)] and a small [<1 μm in diameter; (b)] junction, respectively. A saturated low resistance state (R_p) was observed for both junctions in the high-field regime, presumably corresponding to parallel alignment of the magnetization orientations of the two electrodes. The junctions exhibited higher resistance at low magnetic field, indicative of the deviation of the relative magnetization orientation from parallel alignment. The magnetoresistance of the measured junctions, qualified by $MR \triangleq (R_{\max} - R_p) / R_p$, where $R_{\max}$ is the maximum resistance in the *resistance* vs.f*ield* curve, is presented in the last two columns of Table 3.2. A typical magnetoresistance of 1-4% at low temperatures is found for our junctions, comparable to the 2% magnetoresistance reported in the previous study on high-resistance FM/graphene/FM junctions (*117*).

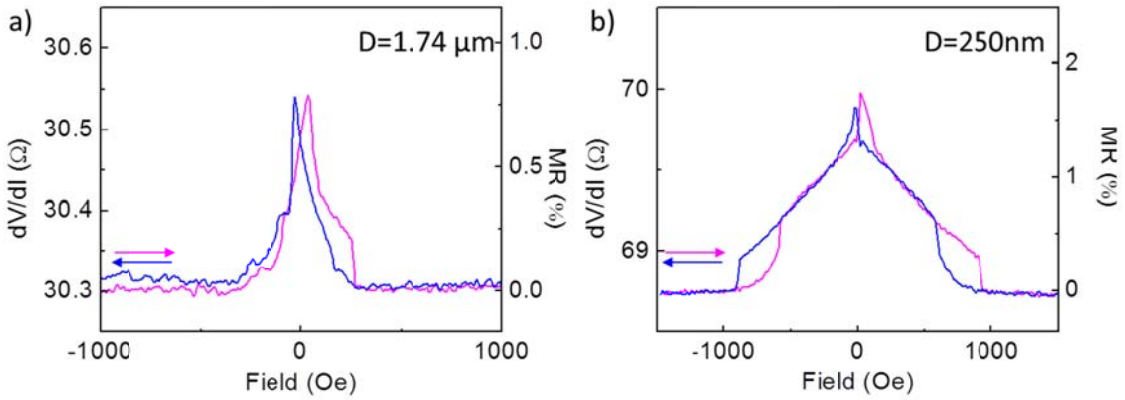

Figure 3.19: Resistance and TMR vs. magnetic field curves of two representative Py/Graphene/Co junctions

(a) A large junction: diameter =1.74 μm; (b) A small junction: diameter =250 nm

For large junctions [Figure 3.19(a)], transitions between the high resistance and low resistance states were observed at relatively low magnetic field strengths (~30 Oe). These values are comparable to the coercive fields of the FM used [15-20 Oe for Co (*130, 131*) and 1-10 Oe for Py (*132*)], indicative of abrupt reverse of magnetization orientations through domain wall motion. For small junctions [Figure 3.19(b)], the magnetoresistance curves feature abrupt changes of the resistance at higher fields on top of a broad lambda-shaped reversible background, indicating that the reverse of magnetic orientation occurs through combinations of discontinuous jumps and coherent magnetization rotations. This interesting *resistance* vs. *field* behavior was consistently observed for all junctions <1 μm in diameter; see for example the data collected on a different device in Figure 3.20(a). In particular, a hysteresis loop corresponding to abrupt magnetization jump of one of the electrodes is found to center at approximately 800 Oe for all small junctions. The relatively large shift of the hysteresis loop from zero field suggests strong antiferromagnetic coupling between the two magnetic electrodes, which is likely caused by dipolar stray-field coupling through the very thin graphene barrier. It should also be pointed out that two recent theoretical studies have indeed suggested the existence of graphene-mediated antiferromagnetic exchange coupling between two magnetic electrodes (*109, 110*).

The detailed reversal process during the measurement can be complex and may depend on domain interactions. We are still working on the possible coherent rotation mechanisms that may account for the lambda-shaped *R-H* relationship at low fields. At the current stage, without knowledge of the detailed magnetization scheme, it's

unclear whether the two electrodes have achieved fully antiparallel magnetization at the maximum resistance point. Consequently, the magnetoresistance presented in Table 3.2 actually represents a lower bound for the highest possible magnetoresistance corresponding to the switch between complete parallel and antiparallel magnetizations.

3.5.4 Temperature and Bias Dependence of the Magnetoresistance

A series of *resistance* vs. *field* curves measured at different bias voltages are displayed in Figure 3.20(a) for another representative device. The magnetoresistance extracted from these curves, again defined by $MR \triangleq (R_{\max} - R_p)/R_p$, is plotted in Figure 3.20 (b). We find that the magnetoresistance depends strongly on the bias voltage: it peaks at low bias voltages and decreases at higher bias voltages. Decreased magnetoresistance at increased biases is typically expected for MTJs. At finite biases, electrons tunnel into the empty states of the receiving electrode with an excess energy, generating phonons and magnons that increase the spin relaxation rate (*133*). Further, the receiving empty states are hot electron states for which the spin polarization is significantly reduced (*134*). These two effects lead to reduction of magnetoresistance at higher bias voltages. The bias voltage dependence of the magnetoresistance exhibits an asymmetry and decreases faster at negative biases when the charge current is injected from the Co electrode into the Py electrode. This asymmetry likely reflects the different density of states for the two different ferromagnetic materials.

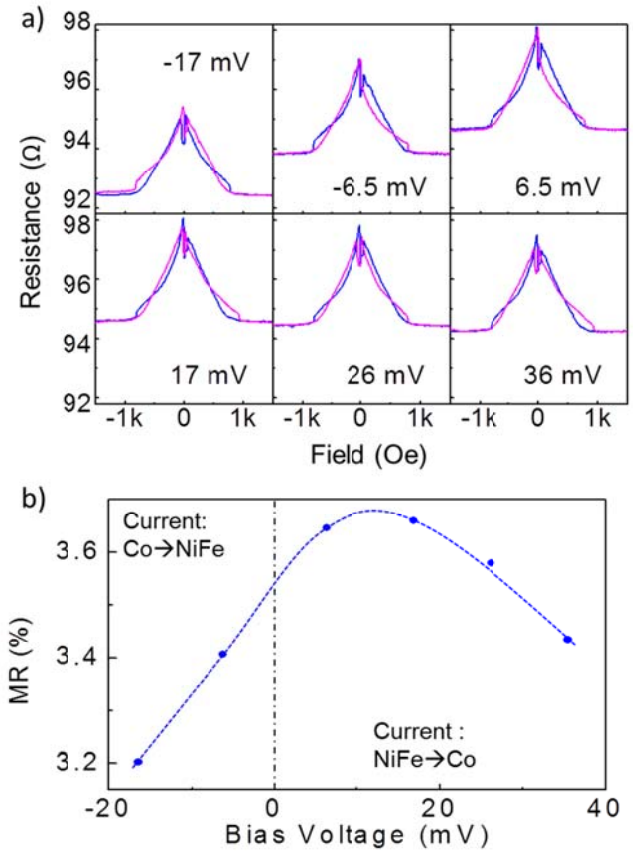

Figure 3.20: Bias dependence of the TMR at low temperature (*T*=6.1K).
(a) *Resistance vs. field* curves measured with a representive Py/Graphene/Co junction at six different bias voltages; (b) A plot of *MR vs. bias voltage* extracted from the curves displayed in Figure (a)

Figure 3.21 shows the temperature dependence of the magnetoresistance of four different devices. Lower magnetoresistance is observed at higher temperature for all four devices. This behavior is typical to MTJs, and can be attributed to the excitation of the spin waves in the ferromagnetic material which decrease the spin polarization (*135*).

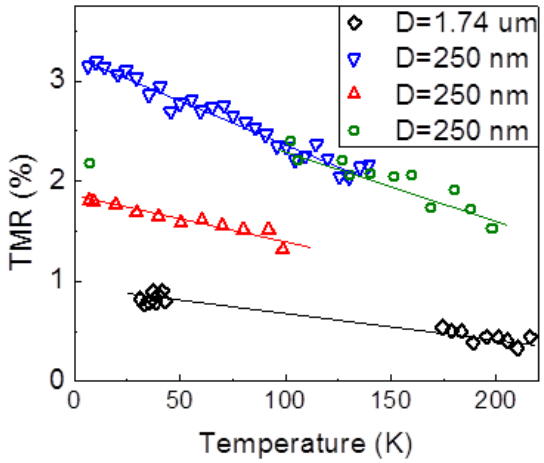

Figure 3.21 : Temperature dependence of TMR for four different devices.

3.5.5 Transport Properties of Control Devices and Devices after Junction Breakdown

Control devices were fabricated and characterized to ensure the signal measured with the test devices comes from the junction area alone. The control devices were fabricated in parallel with the test devices on the same wafer. They have the same structure as the test devices, except that no hole was etched in the Si_3N_4 membrane for the formation of Py/graphene/Co junctions. Figure 3.22 shows the measured *I-V* curve with a control device at room temperature. The *I-V* curve was non-linear, indicative of tunneling transport. The resistance of the control devices was found to be ~30 MΩ, or ~10^6 higher than that of the junctions (typically 10-100 Ω). Thus currents tunneled through the Si_3N_4 membrane are not expected to contribute significantly to the measured data of the Py/graphene/Co junctions.

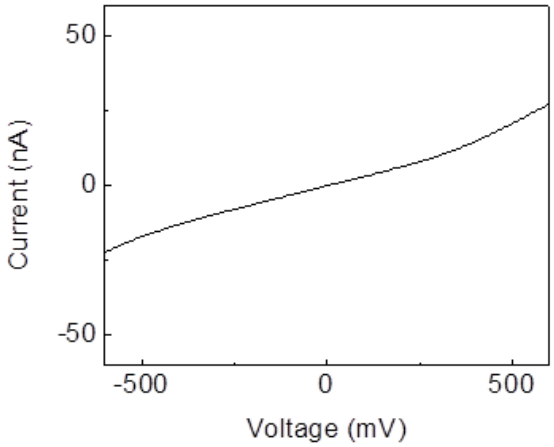

Figure 3.22 : I-V Curve measured with a control device without Py/graphene/Co junction

We have also studied the electrical properties of the Py/graphene/Co junctions after they are broken down with a relatively high DC current. Figure 3.23 shows the bias dependence of the differential resistance of the same junction as presented Figure 3.20 after breakdown. A drop in resistance was found after breakdown, and the differential resistance now *increases* at higher bias voltage, indicative of the formation of point contacts. (*136*)

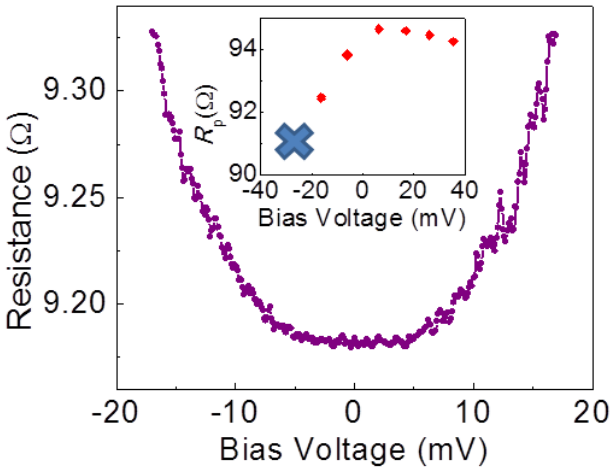

Figure 3.23 : Bias dependence of the junction resistance after junction breakdown.

Inset: Bias dependence of the junction resistance before junction breakdown. The breakdown occurred at a DC current of -0.4 mA, denoted as a cross in the inset image.

3.6 Conclusion

In summary, in this chapter we have discussed our experimental work on FM/graphene/FM junctions. We have developed a fabrication process that aims to realize intrinsic FM/graphene interfaces by preventing oxidation of the ferromagnetic materials at the interface. The fabricated junctions were found to have typical *RA* product of 3-10 $\Omega.\mu m^2$, more than 10^4 times smaller than the values reported by previously experimental studies. Electrical characterizations indicated tunneling transport of junctions with typical magnetoresistance of 1-4%. Nanoscale junction MTJs with low *RA* products could help reduce the *RC* time constant of nano-fabricated devices, which is critical for applications like hard-disk read heads.

3.7 Appendices

3.7.1 Further Discussions on the MR Value Measured with Our Graphene Junctions

The 1-4% MR value measured with our graphene MTJs, while comparable with the previous experimental results from Cobas *et al.(117)*, is significantly lower than the theoretical prediction (~25%) which expected graphene to be an excellent spin filter (*107, 108*). The not-as-big MR value in our experiments is likely due to the lack of a lattice-matched graphene/FM interface, which, in theory, was the prerequisite of the spin filtering effect.

From a theoretical perspective, we notice that the previous theoretical study (*107, 108*) ignored the 1-2% lattice constant difference between graphene and the FM (111) plane. The lattice constant difference is difficult to remove through alloying, as all transition metals have larger lattice constants than graphene. Future theoretical study should thus address this lattice constant difference from more realistic consideration. Prof. Sethna kindly provided a theoretical model which expects graphene on FM (111) plane to form "good" patches with lattice-matched graphene/FM interface, separated by domain walls with misaligned graphene/FM lattices. Under this model, the overall spin filtering effect would be determined by the ratio between the area of the good patches and the area of the domain walls, with thinner domain walls potentially related to a stronger spin filtering effect. In practice, the width of the domain walls could be determined by a combination of the relative stiffness of graphene comparing to FM material and the corrugation potential of graphene on FM (111) plane: A thinner domain wall is expected for high corrugation potential and low graphene stiffness.

Experimentally, CVD graphene has intrinsic domains (*17, 18*), and the evaporation technique we used to deposit FM material on graphene cannot provide epitaxial growth. Both these factors reduced the chances to have lattice-matched graphene/FM in our devices. In fact, despite of the great efforts that have been made in the whole graphene community (*137-142*), a reliable technique to achieve a lattice-matched graphene/FM interface has not yet been developed. A promising method may

be to grow relatively thin FM materials on graphene surfaces, and an intitial attempt of this approach has been demonstrated recently (*143*) (Suggested by Prof. Ralph).

3.7.2 Fabrication Processes to Prepare the Substrate

Figure 3.24 illustrates the fabrication steps we used to prepare the substrate used for FM/graphene/FM junctions (Figure 3.10, step 1). The protocol is adapted from our group's earlier recipes (*121, 122, 144*).

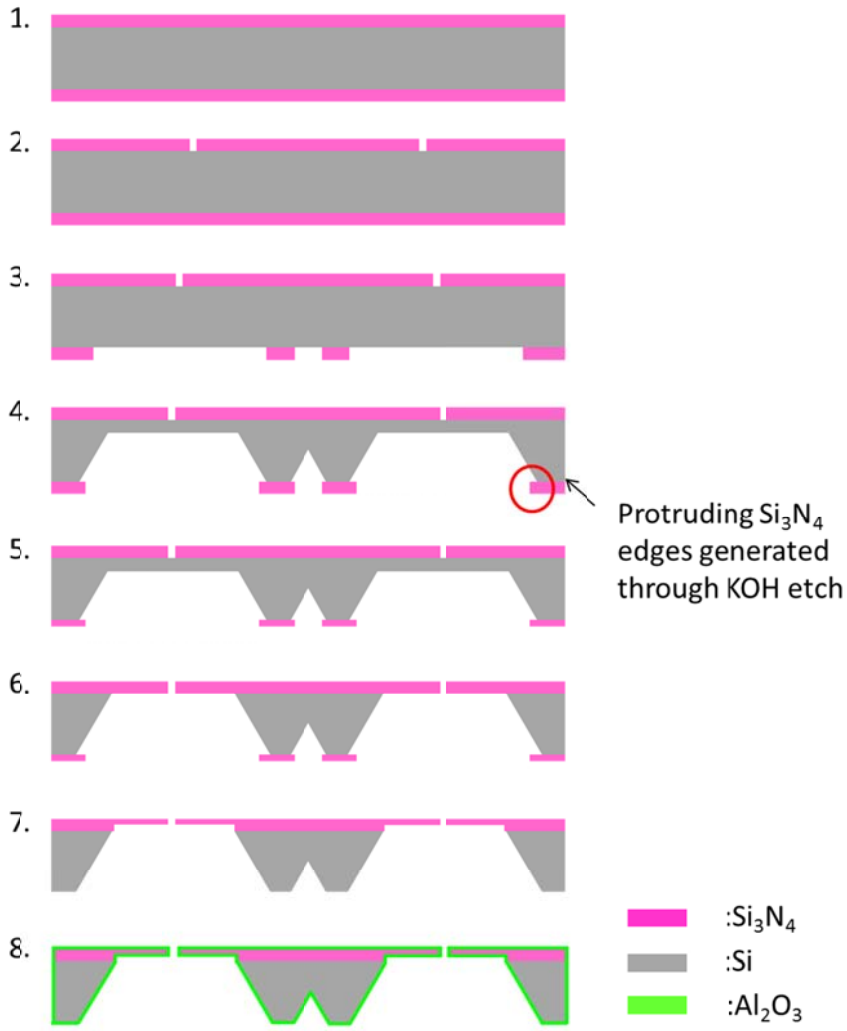

Figure 3.24 : The fabrication process to prepare the substrate.

1. Start with a 4 inch Si (100 direction, 500 μm thick) wafer coated with 300 nm LPCVD Si_3N_4 on both top and bottom surfaces.

2. E-beam lithography (ZEP 520A resist; JEOL 6300) + CHF_3/O_2 plasma etch (Oxford 81 RIE) to pattern the holes on the top Si_3N_4 film which are later used to suspend graphene in Py/graphene/Co junctions.

3. Backside alignment photolithography (Shipley 1813 resist; Suss MA6-BA6 Contact Aligner) + CHF_3/O_2 plasma etch (Oxford 81 RIE) to pattern the windows (760 × 760μm), and trenches (300 μm windows) on bottom Si_3N_4 film which are later used as etch masks in KOH etch steps. The windows are aligned right underneath the holes patterned in step 2. The trenches are designed in between the windows (devices) to make 'V' shaped grooves for device separations.

4. 1st KOH etch (20% KOH at 90^{o}C) to remove 400 μm of Si within the window and the trench region fabricated in Step 2. The etch process will self-terminate in the trenches after 240 μm of Si is removed as a consequence of the designed thickness of trenches in Step 3, leaving the V-shaped grooves between devices for later device separation.

5. CHF_3/O_2 plasma etch (Oxford 81 RIE) from the backside of the wafer to thin down the backside Si_3N_4 to 100 nm.

6. 2nd KOH etch with the rest 100 nm backside Si_3N_4 as etch mask to remove all the Si within the backside Si_3N_4 window to suspend the top Si_3N_4 membrane with holes for suspending graphene.

7. CHF_3/O_2 plasma etch (Oxford 81 RIE) from the backside of the wafer to completely remove the backside Si_3N_4 membrane (over etch designed for 200 nm Si_3N_4). Note that this step also thins down the front side suspended Si_3N_4 to 100 nm.

8. Conformally coat the substrate with 30 nm Al_2O_3 to further ensure electrical isolation between the top and bottom surfaces of the device.

3.7.3 Bias Dependence of the Junction Resistance for more Devices

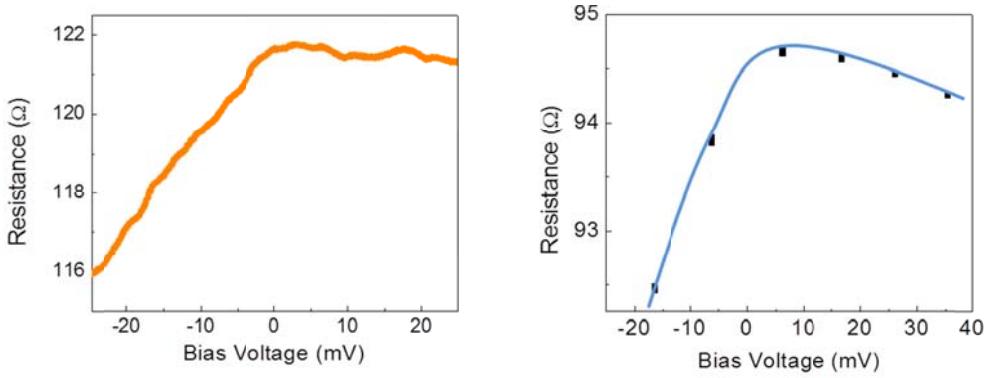

Figure 3.25 : Bias dependence of the junction resistance for more devices.

REFERENCES

1. A. K. Geim, K. S. Novoselov, The rise of graphene. *Nature Materials* **6**, 183 (Mar, 2007).

2. A. H. Castro Neto, F. Guinea, N. M. R. Peres, K. S. Novoselov, A. K. Geim, The electronic properties of graphene. *Reviews of Modern Physics* **81**, 109 (Jan-Mar, 2009).

3. K. S. Novoselov *et al.*, Electric field effect in atomically thin carbon films. *Science* **306**, 666 (Oct, 2004).

4. K. I. Bolotin *et al.*, Ultrahigh electron mobility in suspended graphene. *Solid State Communications* **146**, 351 (Jun, 2008).

5. C. R. Dean *et al.*, Boron nitride substrates for high-quality graphene electronics. *Nature Nanotechnology* **5**, 722 (Oct, 2010).

6. K. S. Novoselov *et al.*, Two-dimensional gas of massless Dirac fermions in graphene. *Nature* **438**, 197 (Nov, 2005).

7. A. B. Kuzmenko, E. van Heumen, F. Carbone, D. van der Marel, Universal optical conductance of graphite. *Phys. Rev. Lett.* **100**, (Mar, 2008).

8. C. Lee, X. D. Wei, J. W. Kysar, J. Hone, Measurement of the elastic properties and intrinsic strength of monolayer graphene. *Science* **321**, 385 (Jul, 2008).

9. S. S. Chen *et al.*, Raman measurements of thermal transport in suspended monolayer graphene of variable sizes in vacuum and gaseous environments. *Acs Nano* **5**, 321 (Jan, 2011).

10. A. A. Balandin, Thermal properties of graphene and nanostructured carbon materials. *Nature Materials* **10**, 569 (Aug, 2011).

11. E. Pop, V. Varshney, A. K. Roy, Thermal properties of graphene: Fundamentals and applications. *Mrs Bulletin* **37**, 1273 (Dec, 2012).

12. K. S. Novoselov *et al.*, A roadmap for graphene. *Nature* **490**, 192 (Oct, 2012).

13. W. Li, C. Tan, M. A. Lowe, H. D. Abruna, D. C. Ralph, Electrochemistry of individual monolayer graphene sheets. *Acs Nano* **5**, 2264 (Mar, 2011).

14. A. S. Mayorov *et al.*, Micrometer-scale ballistic transport in encapsulated graphene at room temperature. *Nano Lett.* **11**, 2396 (Jun, 2011).

15. X. S. Li *et al.*, Large-area synthesis of high-quality and uniform graphene films on copper foils. *Science* **324**, 1312 (Jun, 2009).

16. Y. Lee *et al.*, Wafer-scale synthesis and transfer of graphene films. *Nano Lett.* **10**, 490 (Feb, 2010).

17. P. Y. Huang *et al.*, Grains and grain boundaries in single-layer graphene atomic patchwork quilts. *Nature* **469**, 389 (Jan 20, 2011).

18. K. Kim *et al.*, Grain boundary mapping in polycrystalline graphene. *Acs Nano* **5**, 2142 (Mar, 2011).

19. N. Petrone *et al.*, Chemical vapor deposition-derived graphene with electrical performance of exfoliated graphene. *Nano Lett.* **12**, 2751 (Jun, 2012).

20. W. Gannett *et al.*, Boron nitride substrates for high mobility chemical vapor deposited graphene. *Appl. Phys. Lett.* **98**, (Jun, 2011).

21. A. Avsar *et al.*, Toward wafer scale fabrication of graphene based spin valve devices. *Nano Lett.* **11**, 2363 (Jun, 2011).

22. H. L. Cao *et al.*, Electronic transport in chemical vapor deposited graphene synthesized on Cu: Quantum Hall effect and weak localization. *Appl. Phys. Lett.* **96**, (Mar, 2010).

23. Y. Hernandez *et al.*, High-yield production of graphene by liquid-phase exfoliation of graphite. *Nature Nanotechnology* **3**, 563 (Sep, 2008).

24. M. Lotya *et al.*, Liquid phase production of graphene by exfoliation of graphite in surfactant/water solutions. *Journal of the American Chemical Society* **131**, 3611 (Mar, 2009).

25. S. Stankovich *et al.*, Synthesis of graphene-based nanosheets via chemical reduction of exfoliated graphite oxide. *Carbon* **45**, 1558 (Jun, 2007).

26. A. B. Bourlinos *et al.*, Graphite oxide: Chemical reduction to graphite and surface modification with primary aliphatic amines and amino acids. *Langmuir* **19**, 6050 (Jul, 2003).

27. Y. Y. Shao *et al.*, Graphene based electrochemical sensors and biosensors: A review. *Electroanalysis* **22**, 1027 (May, 2010).

28. S. Alwarappan, A. Erdem, C. Liu, C. Z. Li, Probing the electrochemical properties of graphene nanosheets for biosensing applications. *Journal of Physical Chemistry C* **113**, 8853 (May, 2009).

29. M. Zhou, Y. M. Zhai, S. J. Dong, Electrochemical sensing and biosensing platform based on chemically reduced graphene oxide. *Analytical Chemistry* **81**, 5603 (Jul, 2009).

30. Y. Wang, Y. Y. Shao, D. W. Matson, J. H. Li, Y. H. Lin, Nitrogen-doped graphene and its application in electrochemical biosensing. *Acs Nano* **4**, 1790 (Apr, 2010).

31. X. H. Kang *et al.*, A graphene-based electrochemical sensor for sensitive detection of paracetamol. *Talanta* **81**, 754 (May, 2010).

32. L. H. Tang *et al.*, Preparation, Structure, and Electrochemical Properties of Reduced Graphene Sheet Films. *Advanced Functional Materials* **19**, 2782 (Sep, 2009).

33. X. L. Li *et al.*, Highly conducting graphene sheets and Langmuir-Blodgett films. *Nature Nanotechnology* **3**, 538 (Sep, 2008).

34. L. J. Cote, F. Kim, J. Huang, Langmuir-Blodgett Assembly of Graphite Oxide Single Layers. *Journal of the American Chemical Society* **131**, 1043 (Jan 28, 2009).

35. X. Wang, L. J. Zhi, K. Mullen, Transparent, conductive graphene electrodes for dye-sensitized solar cells. *Nano Lett.* **8**, 323 (Jan, 2008).

36. K. S. Kim *et al.*, Large-scale pattern growth of graphene films for stretchable transparent electrodes. *Nature* **457**, 706 (Feb 5, 2009).

37. H. Park, P. R. Brown, V. Buloyic, J. Kong, Graphene as transparent conducting electrodes in organic photovoltaics: studies in graphene morphology, hole transporting layers, and counter electrodes. *Nano Lett.* **12**, 133 (Jan, 2012).

38. R. W. Murray, Roses and raspberries. *Analytical Chemistry* **82**, 3405 (May, 2010).

39. F. Schedin *et al.*, Detection of individual gas molecules adsorbed on graphene. *Nature Materials* **6**, 652 (Sep, 2007).

40. H. T. Liu, Y. Q. Liu, D. B. Zhu, Chemical doping of graphene. *Journal of Materials Chemistry* **21**, 3335 (2011).

41. W. Chen, S. Chen, D. C. Qi, X. Y. Gao, A. T. S. Wee, Surface transfer p-type doping of epitaxial graphene. *Journal of the American Chemical Society* **129**, 10418 (Aug, 2007).

42. S. Y. Zhou, D. A. Siegel, A. V. Fedorov, A. Lanzara, Metal to insulator transition in epitaxial graphene induced by molecular doping. *Phys. Rev. Lett.* **101**, (Aug, 2008).

43. D. C. Elias *et al.*, Control of graphene's properties by reversible hydrogenation: Evidence for graphane. *Science* **323**, 610 (Jan, 2009).

44. A. Sinitskii *et al.*, Kinetics of diazonium functionalization of chemically convertedgraphene nanoribbons. *Acs Nano* **4**, 1949 (Apr, 2010).

45. H. M. Jeong *et al.*, Nitrogen-doped graphene for high-performance ultracapacitors and the importance of nitrogen-doped sites at basal planes. *Nano Lett.* **11**, 2472 (Jun, 2011).

46. C. G. Liu, Z. N. Yu, D. Neff, A. Zhamu, B. Z. Jang, Graphene-based supercapacitor with an ultrahigh energy density. *Nano Lett.* **10**, 4863 (Dec, 2010).

47. M. D. Stoller, S. J. Park, Y. W. Zhu, J. H. An, R. S. Ruoff, Graphene-Based Ultracapacitors. *Nano Lett.* **8**, 3498 (Oct, 2008).

48. V. Georgakilas *et al.*, Multipurpose organically modified carbon nanotubes: From functionalization to nanotube composites. *Journal of the American Chemical Society* **130**, 8733 (Jul, 2008).

49. A. Das *et al.*, Monitoring dopants by Raman scattering in an electrochemically top-gated graphene transistor. *Nature Nanotechnology* **3**, 210 (Apr, 2008).

50. X. Ling *et al.*, Can graphene be used as a substrate for Raman enhancement? *Nano Lett.* **10**, 553 (Feb, 2010).

51. J. T. Robinson *et al.*, Properties of fluorinated graphene films. *Nano Lett.* **10**, 3001 (Aug, 2010).

52. Q. H. Wang, M. C. Hersam, Room-temperature molecular-resolution characterization of self-assembled organic monolayers on epitaxial graphene. *Nature Chemistry* **1**, 206 (Jun, 2009).

53. A. J. Bard, L. R. Faulkner, *Electrochemical methods: Fundamentals and applications*. (Wiley, ed. 2, 2000).

54. J. Heinze, Ultramicroelectrodes in electrochemistry. *Angewandte Chemie-International Edition in English* **32**, 1268 (Sep, 1993).

55. I. Heller *et al.*, Individual single-walled carbon nanotubes as nanoelectrodes for electrochemistry. *Nano Lett.* **5**, 137 (Jan, 2005).

56. Nicholson.Rs, Theory and application of cyclic voltammetry for measurement of electrode reaction kinetics. *Analytical Chemistry* **37**, 1351 (1965).

57. M. Julliere, Tunneling between ferromagnetic-films. *Physics Letters A* **54**, 225 (1975).

58. S. Ikeda *et al.*, Tunnel magnetoresistance of 604% at 300 K by suppression of Ta diffusion in CoFeB/MgO/CoFeB pseudo-spin-valves annealed at high temperature. *Appl. Phys. Lett.* **93**, (Aug, 2008).

59. J. G. J. Zhu, C. D. Park, Magnetic tunnel junctions. *Materials Today* **9**, 36 (Nov, 2006).

60. S. Yuasa, D. D. Djayaprawira, Giant tunnel magnetoresistance in magnetic tunnel junctions with a crystalline MgO(001) barrier. *Journal of Physics D-Applied Physics* **40**, R337 (Nov, 2007).

61. D. C. Ralph, M. D. Stiles, Spin transfer torques. *Journal of Magnetism and Magnetic Materials* **320**, 1190 (Apr, 2008).

62. Y. Nagamine *et al.*, Ultralow resistance-area product of 0.4 Omega(mu m)(2) and high magnetoresistance above 50% in CoFeB/MgO/CoFeB magnetic tunnel junctions. *Appl. Phys. Lett.* **89**, (Oct, 2006).

63. Z. S. Li, C. de Groot, J. H. Moodera, Gallium oxide as an insulating barrier for spin-dependent tunneling junctions. *Appl. Phys. Lett.* **77**, 3630 (Nov, 2000).

64. J. J. Sun *et al.*, Low resistance and high thermal stability of spin-dependent tunnel junctions with synthetic antiferromagnetic CoFe/Ru/CoFe pinned layers. *Appl. Phys. Lett.* **76**, 2424 (Apr, 2000).

65. S. N. Mao *et al.*, Tunneling magnetoresistive heads beyond 150 Gb/in(2). *Ieee Transactions on Magnetics* **40**, 307 (Jan, 2004).

66. T. Kuwashima *et al.*, Electrical performance and reliability of tunnel magnetoresistance heads for 100-Gb/in(2) application. *Ieee Transactions on Magnetics* **40**, 176 (Jan, 2004).

67. K. Yakushiji *et al.*, High magnetoresistance ratio and low resistance-area product in magnetic tunnel junctions with perpendicularly magnetized electrodes. *Applied Physics Express* **3**, (2010).

68. S. Isogami *et al.*, In situ heat treatment of ultrathin MgO layer for giant magnetoresistance ratio with low resistance area product in CoFeB/MgO/CoFeB magnetic tunnel junctions. *Appl. Phys. Lett.* **93**, (Nov, 2008).

69. J. M. Pomeroy, H. Grube, A. C. Perrella, J. D. Gillaspy, Selectable resistance-area product by dilute highly charged ion irradiation. *Appl. Phys. Lett.* **91**, (Aug, 2007).

70. Nicholso.Rs, Theory and application of cyclic voltammetry for measurement of electrode reaction kinetics. *Analytical Chemistry* **37**, 1351 (1965, 1965).

71. K. B. Oldham, J. C. Myland, C. G. Zoski, A. M. Bond, Kinetic-parameters from steady-state voltammograms at microdisc electrodes. *Journal of Electroanalytical Chemistry* **270**, 79 (Oct 10, 1989).

72. R. L. McCreery, Advanced carbon electrode materials for molecular electrochemistry. *Chemical Reviews* **108**, 2646 (Jul, 2008).

73. J. K. Campbell, L. Sun, R. M. Crooks, Electrochemistry using single carbon nanotubes. *Journal of the American Chemical Society* **121**, 3779 (Apr, 1999).

74. J. Chlistunoff, D. Cliffel, A. J. Bard, Electrochemistry of fullerene films. *Thin Solid Films* **257**, 166 (Mar, 1995).

75. S. Alehashem, F. Chambers, J. W. Strojek, G. M. Swain, R. Ramesham, Cyclic voltammetric studies of charge-transfer reactions at highly boron-doped polycrystalline diamond thin-film electrodes. *Analytical Chemistry* **67**, 2812 (Sep, 1995).

76. Y. V. Pleskov, Electrochemistry of diamond: A review. *Russian Journal of Electrochemistry* **38**, 1275 (Dec, 2002).

77. K. S. Novoselov *et al.*, Two-dimensional atomic crystals. *Proceedings of the National Academy of Sciences of the United States of America* **102**, 10451 (Jul, 2005).

78. E. Watanabe, A. Conwill, D. Tsuya, Y. Koide, Low contact resistance metals for graphene based devices. *Diamond and Related Materials* **24**, 171 (Apr, 2012).

79. K. Nagashio, T. Nishimura, K. Kita, A. Toriumi, Contact resistivity and current flow path at metal/graphene contact. *Appl. Phys. Lett.* **97**, (Oct, 2010).

80. A. C. Ferrari *et al.*, Raman spectrum of graphene and graphene layers. *Phys. Rev. Lett.* **97**, (Nov, 2006).

81. M. P. Levendorf, C. S. Ruiz-Vargas, S. Garg, J. Park, Transfer-Free Batch Fabrication of Single Layer Graphene Transistors. *Nano Lett.* **9**, 4479 (Dec, 2009).

82. M. V. Mirkin, A. J. Bard, Simple analysis of quasi-reversible steady-state voltammograms. *Analytical Chemistry* **64**, 2293 (Oct, 1992).

83. A. V. Patil *et al.*, Fabrication and characterization of polymer insulated carbon nanotube modified electrochemical nanoprobes. *Nanoscale* **2**, 734 (2010, 2010).

84. R. M. Nielson, G. E. McManis, L. K. Safford, M. J. Weaver, Solvent and electrolyte effects on the kinetics of ferrocenium ferrocene self-exchange - A reevaluation. *Journal of Physical Chemistry* **93**, 2152 (Mar, 1989).

85. K. K. Cline, M. T. McDermott, R. L. McCreery, Anomalously slow-electron transfer at ordered graphite-electrodes - Influence of electronic factors and reactive sites. *Journal of Physical Chemistry* **98**, 5314 (May, 1994).

86. S. Niyogi *et al.*, Chemistry of single-walled carbon nanotubes. *Accounts of Chemical Research* **35**, 1105 (Dec, 2002).

87. S. Ryu *et al.*, Reversible basal plane hydrogenation of graphene. *Nano Lett.* **8**, 4597 (Dec, 2008).

88. J. C. Meyer *et al.*, The structure of suspended graphene sheets. *Nature* **446**, 60 (Mar, 2007).

89. M. Ishigami, J. H. Chen, W. G. Cullen, M. S. Fuhrer, E. D. Williams, Atomic structure of graphene on SiO2. *Nano Lett.* **7**, 1643 (Jun, 2007).

90. K. Xu, P. G. Cao, J. R. Heath, Scanning tunneling microscopy characterization of the electrical properties of wrinkles in exfoliated graphene monolayers. *Nano Lett.* **9**, 4446 (Dec, 2009).

91. F. Guinea, M. I. Katsnelson, M. A. H. Vozmediano, Midgap states and charge inhomogeneities in corrugated graphene. *Phys. Rev. B* **77**, (Feb, 2008).

92. M. E. Williams, J. T. Hupp, Scanning electrochemical microscopy assessment of rates of molecular transport through mesoporous thin-films of porphyrinic "Molecular squares". *Journal of Physical Chemistry B* **105**, 8944 (Sep, 2001).

93. D. Zheng, H. H. Li, B. Y. Lu, Z. H. Xu, H. Y. Chen, Electrochemical properties of ferrocene adsorbed on multi-walled carbon nanotubes electrode. *Thin Solid Films* **516**, 2151 (Feb, 2008).

94. C. Tan *et al.*, Reactivity of monolayer chemical vapor deposited graphene imperfections studied using scanning electrochemical microscopy. *Acs Nano* **6**, 3070 (Apr, 2012).

95. R. L. McCreery, M. T. McDermott, Comment on electrochemical kinetics at ordered graphite electrodes. *Analytical Chemistry* **84**, 2602 (Mar, 2012).

96. N. L. Ritzert, J. Rodriguez-Lopez, C. Tan, H. D. Abruna, Kinetics of interfacial electron transfer at single-layer graphene electrodes in aqueous and nonaqueous solutions. *Langmuir* **29**, 1683 (Feb, 2013).

97. A. T. Valota *et al.*, Electrochemical behavior of monolayer and bilayer graphene. *Acs Nano* **5**, 8809 (Nov, 2011).

98. J. A. Mann, J. Rodriguez-Lopez, H. D. Abruna, W. R. Dichtel, Multivalent binding motifs for the noncovalent functionalization of graphene. *Journal of the American Chemical Society* **133**, 17614 (Nov, 2011).

99. A. P. Brown, F. C. Anson, Cyclic and differential pulse voltammetric behavior of reactants confined to electrode surface. *Analytical Chemistry* **49**, 1589 (1977).

100. S. S. P. Parkin *et al.*, Giant tunnelling magnetoresistance at room temperature with MgO (100) tunnel barriers. *Nature Materials* **3**, 862 (Dec, 2004).

101. D. X. Wang, C. Nordman, J. M. Daughton, Z. H. Qian, J. Fink, 70% TMR at room temperature for SDT sandwich junctions with CoFeB as free and reference layers. *Ieee Transactions on Magnetics* **40**, 2269 (Jul, 2004).

102. S. Yuasa, T. Nagahama, A. Fukushima, Y. Suzuki, K. Ando, Giant room-temperature magnetoresistance in single-crystal Fe/MgO/Fe magnetic tunnel junctions. *Nature Materials* **3**, 868 (Dec, 2004).

103. T. Miyazaki, N. Tezuka, Giant magnetic tunneling effect in Fe/Al2O3/Fe junction. *Journal of Magnetism and Magnetic Materials* **139**, L231 (Jan, 1995).

104. J. S. Moodera, L. R. Kinder, T. M. Wong, R. Meservey, Large magnetoresistance at room-temperature in ferromagnetic thin-film tunnel-junctions. *Phys. Rev. Lett.* **74**, 3273 (Apr, 1995).

105. W. H. Butler, X. G. Zhang, T. C. Schulthess, J. M. MacLaren, Spin-dependent tunneling conductance of Fe vertical bar MgO vertical bar Fe sandwiches. *Phys. Rev. B* **63**, (Feb, 2001).

106. J. Mathon, A. Umerski, Theory of tunneling magnetoresistance of an epitaxial Fe/MgO/Fe(001) junction. *Phys. Rev. B* **63**, (Jun, 2001).

107. V. M. Karpan *et al.*, Graphite and graphene as perfect spin filters. *Phys. Rev. Lett.* **99**, (Oct, 2007).

108. V. M. Karpan *et al.*, Theoretical prediction of perfect spin filtering at interfaces between close-packed surfaces of Ni or Co and graphite or graphene. *Phys. Rev. B* **78**, (Nov, 2008).

109. D. Kim, A. Hashmi, C. Hwang, J. Hong, Magnetization reversal and spintronics of Ni/Graphene/Co induced by doped graphene. *Appl. Phys. Lett.* **102**, (Mar, 2013).

110. D. Kim, J. Yang, J. Hong, C. Hwang, R. Q. Wu, Carrier-induced spin switching in Co/Graphene/Ni: A first principles study. *Journal of the Korean Physical Society* **60**, 420 (Feb, 2012).

111. K. K. Saha, A. Blom, K. S. Thygesen, B. K. Nikolic, Magnetoresistance and negative differential resistance in Ni/graphene/Ni vertical heterostructures driven by finite bias voltage: A first-principles study. *Phys. Rev. B* **85**, (May, 2012).

112. R. Sato, T. Hiraiwa, J. Inoue, S. Honda, H. Itoh, Magnetoresistance in fcc Ni/graphene/fcc Ni(111) junctions. *Phys. Rev. B* **85**, (Mar, 2012).

113. N. Tombros, C. Jozsa, M. Popinciuc, H. T. Jonkman, B. J. van Wees, Electronic spin transport and spin precession in single graphene layers at room temperature. *Nature* **448**, 571 (Aug, 2007).

114. W. Han *et al.*, Tunneling spin injection into single layer graphene. *Phys. Rev. Lett.* **105**, (Oct, 2010).

115. B. Dlubak *et al.*, Highly efficient spin transport in epitaxial graphene on SiC. *Nature Physics* **8**, 557 (Jul, 2012).

116. E. W. Hill, A. K. Geim, K. Novoselov, F. Schedin, P. Blake, Graphene spin valve devices. *Ieee Transactions on Magnetics* **42**, 2694 (Oct, 2006).

117. E. Cobas, A. L. Friedman, O. M. J. van't Erve, J. T. Robinson, B. T. Jonker, Graphene as a tunnel barrier: graphene-based magnetic tunnel junctions. *Nano Lett.* **12**, 3000 (Jun, 2012).

118. W. Sheng, Z. Y. Ning, Z. Q. Yang, H. Guo, Magnetism and perfect spin filtering effect in graphene nanoflakes. *Nanotechnology* **21**, (Sep, 2010).

119. B. H. Li, L. A. Chen, X. Q. Pan, Spin-flip phenomena at the Co vertical bar graphene vertical bar Co interfaces. *Appl. Phys. Lett.* **98**, (Mar, 2011).

120. S. S. Chen *et al.*, Oxidation resistance of graphene-coated Cu and Cu/Ni alloy. *Acs Nano* **5**, 1321 (Feb, 2011).

121. S. Gueron, M. M. Deshmukh, E. B. Myers, D. C. Ralph, Tunneling via individual electronic states in ferromagnetic nanoparticles. *Phys. Rev. Lett.* **83**, 4148 (Nov, 1999).

122. D. C. Ralph, C. T. Black, M. Tinkham, Spectroscopic measurements of discrete electronic states in single metal particles. *Phys. Rev. Lett.* **74**, 3241 (Apr, 1995).

123. O. V. Yazyev, S. G. Louie, Electronic transport in polycrystalline graphene. *Nature Materials* **9**, 806 (Oct, 2010).

124. A. W. Tsen *et al.*, Tailoring electrical transport across grain boundaries in polycrystalline graphene. *Science* **336**, 1143 (Jun, 2012).

125. S. M. Sze, K. K. Ng, *Physics of semiconductor devices*. (John Wiley & Sons Inc., Hoboken, New Jersey, 2007).

126. W. F. Brinkman, R. C. Dynes, J. M. Rowell, Tunneling conductance of asymmetrical barriers. *Journal of Applied Physics* **41**, 1915 (1970).

127. F. Guinea, Spin-flip scattering in magnetic junctions. *Phys. Rev. B* **58**, 9212 (Oct, 1998).

128. J. S. Moodera, G. Mathon, Spin polarized tunneling in ferromagnetic junctions. *Journal of Magnetism and Magnetic Materials* **200**, 248 (Oct, 1999).

129. B. J. Jonsson-Akerman *et al.*, Reliability of normal-state current-voltage characteristics as an indicator of tunnel-junction barrier quality. *Appl. Phys. Lett.* **77**, 1870 (Sep, 2000).

130. Z. G. Sun, H. Akinaga, Enhanced coercive field of cobalt film deposited on noodle-like porous silicon substrates. *Appl. Phys. Lett.* **86**, (May, 2005).

131. M. Lohndorf, A. Wadas, H. A. M. vandenBerg, R. Wiesendanger, Structure of cross-tie wall in thin Co films resolved by magnetic force microscopy. *Appl. Phys. Lett.* **68**, 3635 (Jun, 1996).

132. E. E. Huber, D. O. Smith, J. B. Goodenough, Domain-wall structure in permalloy films. *Journal of Applied Physics* **29**, 294 (1958).

133. S. Zhang, P. M. Levy, A. C. Marley, S. S. P. Parkin, Quenching of magnetoresistance by hot electrons in magnetic tunnel junctions. *Phys. Rev. Lett.* **79**, 3744 (Nov, 1997).

134. S. O. Valenzuela, D. J. Monsma, C. M. Marcus, V. Narayanamurti, M. Tinkham, Spin polarized tunneling at finite bias. *Phys. Rev. Lett.* **94**, (May, 2005).

135. C. H. Shang, J. Nowak, R. Jansen, J. S. Moodera, Temperature dependence of magnetoresistance and surface magnetization in ferromagnetic tunnel, junctions. *Phys. Rev. B* **58**, R2917 (Aug, 1998).

136. A. M. Duif, A. G. M. Jansen, P. Wyder, Point-contact spectroscopy. *Journal of Physics-Condensed Matter* **1**, 3157 (May, 1989).

137. D. Eom *et al.*, Structure and electronic properties of graphene nanoislands on Co(0001). *Nano Lett.* **9**, 2844 (Aug, 2009).

138. W. Zhao *et al.*, Graphene on Ni(111): Coexistence of different surface structures. *Journal of Physical Chemistry Letters* **2**, 759 (Apr, 2011).

139. Y. Murata *et al.*, Moire superstructures of graphene on faceted nickel islands. *Acs Nano* **4**, 6509 (Nov, 2010).

140. S. Grandthyll *et al.*, Epitaxial growth of graphene on transition metal surfaces: chemical vapor deposition versus liquid phase deposition. *Journal of Physics-Condensed Matter* **24**, (Aug, 2012).

141. Y. S. Dedkov, M. Fonin, Electronic and magnetic properties of the graphene-ferromagnet interface. *New Journal of Physics* **12**, (Dec, 2010).

142. Y. F. Zhang *et al.*, Different growth behaviors of ambient pressure chemical vapor deposition graphene on Ni(111) and Ni films: A scanning tunneling microscopy study. *Nano Research* **5**, 402 (Jun, 2012).

143. C. Vo-Van *et al.*, Ultrathin epitaxial cobalt films on graphene for spintronic investigations and applications. *New Journal of Physics* **12**, (Oct, 2010).

144. C. T. Black, D. C. Ralph, M. Tinkham, Spectroscopy of the superconducting gap in individual nanometer-scale aluminum particles. *Phys. Rev. Lett.* **76**, 688 (Jan, 1996).